



Citation for published version:

Tadaki, K, Belli, S, Burkert, A, Dekel, A, Förster Schreiber, NM, Genzel, R, Hayashi, M, Herrera-camus, R, Kodama, T, Kohno, K, Koyama, Y, Lee, MM, Lutz, D, Mowla, L, Nelson, EJ, Renzini, A, Suzuki, TL, Tacconi, LJ, Übler, H, Wisnioski, E & Wuyts, S 2020, 'Structural Evolution in Massive Galaxies at $z \sim 2$ ', *The Astrophysical Journal*, vol. 901, no. 1, 74. <https://doi.org/10.3847/1538-4357/abaf4a>

DOI:

[10.3847/1538-4357/abaf4a](https://doi.org/10.3847/1538-4357/abaf4a)

Publication date:

2020

Document Version

Peer reviewed version

[Link to publication](#)

This is an author-created, un-copyedited version of an article published in [insert name of journal]. IOP Publishing Ltd is not responsible for any errors or omissions in this version of the manuscript or any version derived from it. The Version of Record is available online at <https://doi.org/10.3847/1538-4357/abaf4a>.

University of Bath

General rights

Copyright and moral rights for the publications made accessible in the public portal are retained by the authors and/or other copyright owners and it is a condition of accessing publications that users recognise and abide by the legal requirements associated with these rights.

Take down policy

If you believe that this document breaches copyright please contact us providing details, and we will remove access to the work immediately and investigate your claim.

STRUCTURAL EVOLUTION IN MASSIVE GALAXIES AT $Z \sim 2$

KEN-ICHI TADAKI¹, SIRIO BELLI², ANDREAS BURKERT^{3,4}, AVISHAI DEKEL⁵, NATASCHA M. FÖRSTER SCHREIBER⁴, REINHARD GENZEL⁴, MASAO HAYASHI¹, RODRIGO HERRERA-CAMUS⁶, TADAYUKI KODAMA⁷, KOTARO KOHNO^{8,9}, YUSEI KOYAMA¹, MINJU M. LEE⁴, DIETER LUTZ⁴, LAMIYA MOWLA¹⁰, ERICA J. NELSON², ALVIO RENZINI¹¹, TOMOKO L. SUZUKI⁷, LINDA J. TACCONI⁴, HANNAH ÜBLER⁴, EMILY WISNIOSKI^{12,13}, STIJN WUYTS¹⁴

¹ National Astronomical Observatory of Japan, 2-21-1 Osawa, Mitaka, Tokyo 181-8588, Japan; tadaki.ken@nao.ac.jp

² Harvard-Smithsonian Center for Astrophysics, 60 Garden Street, Cambridge, MA 02138, USA

³ Universitäts-Sternwarte Ludwig-Maximilians-Universität (USM), Scheinerstr. 1, München, D-81679, Germany

⁴ Max-Planck-Institut für extraterrestrische Physik, Giessenbachstrasse, D-85748 Garching, Germany

⁵ Racah Institute of Physics, The Hebrew University, Jerusalem 91904 Israel

⁶ Astronomy Department, Universidad de Concepción, Barrio Universitario, Concepción, Chile

⁷ Astronomical Institute, Tohoku University, 6-3, Aramaki, Aoba, Sendai, Miyagi, 980-8578, Japan

⁸ Institute of Astronomy, School of Science, The University of Tokyo, 2-21-1 Osawa, Mitaka, Tokyo 181-0015, Japan

⁹ Research Center for the Early Universe, School of Science, The University of Tokyo, 7-3-1 Hongo, Bunkyo, Tokyo 113-0033, Japan

¹⁰ Astronomy Department, Yale University, 52 Hillhouse Avenue, New Haven, CT 06511, USA

¹¹ INAF - Osservatorio Astronomico di Padova, Vicolo dell'Osservatorio 5, I-35122 Padova, Italy

¹² Research School of Astronomy and Astrophysics, Australian National University, Canberra, ACT 2611, Australia

¹³ ARC Centre of Excellence for All Sky Astrophysics in 3 Dimensions (ASTRO 3D), Australia and

¹⁴ Department of Physics, University of Bath, Claverton Down, Bath, BA2 7AY, UK

Draft version September 7, 2020

ABSTRACT

We present $0''.2$ -resolution Atacama Large Millimeter/submillimeter Array observations at $870 \mu\text{m}$ in a stellar mass-selected sample of 85 massive ($M_\star > 10^{11} M_\odot$) star-forming galaxies (SFGs) at $z = 1.9 - 2.6$ in the 3D-HST/CANDELS fields of UDS and GOODS-S. We measure the effective radius of the rest-frame far-infrared (FIR) emission for 62 massive SFGs. They are distributed over wide ranges of FIR size from $R_{\text{e,FIR}} = 0.4 \text{ kpc}$ to $R_{\text{e,FIR}} = 6 \text{ kpc}$. The effective radius of the FIR emission is smaller by a factor of $2.3_{-1.0}^{+1.9}$ than the effective radius of the optical emission and by a factor of $1.9_{-1.0}^{+1.9}$ smaller than the half-mass radius. Even with taking into account potential extended components, the FIR size would change by $\sim 10\%$. By combining the spatial distributions of the FIR and optical emission, we investigate how galaxies change the effective radius of the optical emission and the stellar mass within a radius of 1 kpc, $M_{1\text{kpc}}$. The compact starburst puts most of massive SFGs on the mass-size relation for quiescent galaxies (QGs) at $z \sim 2$ within 300 Myr if the current star formation activity and its spatial distribution are maintained. We also find that within 300 Myr, $\sim 38\%$ of massive SFGs can reach the central mass of $M_{1\text{kpc}} = 10^{10.5} M_\odot$, which is around the boundary between massive SFGs and QGs. These results suggest an outside-in transformation scenario in which a dense core is formed at the center of a more extended disk, likely via dissipative in-disk inflows. Synchronized observations at ALMA $870 \mu\text{m}$ and *JWST* $3-4 \mu\text{m}$ will explicitly verify this scenario.

Keywords: galaxies: starburst — galaxies: high-redshift — galaxies: ISM

1. INTRODUCTION

In the current Universe, the most massive ($M_\star > 10^{11} M_\odot$) galaxies are spheroids or have a prominent bulge in the center (e.g., Conselice 2014) and show little ongoing star formation activity (e.g., Peng et al. 2010). One of the ultimate challenges in galaxy formation and evolution is to understand how massive galaxies obtained a bulge-dominated morphology and stopped forming stars. In this paper, we focus especially on the structural evolution in massive galaxies at $z \sim 2$, when the cosmic star formation history peaks (e.g., Madau & Dickinson 2014).

Surface brightness profiles of galaxies are well described by Sérsic models (Sérsic 1963),

$$I(r) \propto \exp[-b_n \left(\frac{r}{R_e}\right)^{1/n} - 1] \quad (1)$$

where R_e is the effective radius, n is the Sérsic index

($n = 0.5$ for Gaussian, $n = 1$ for an exponential profile, $n = 4$ for de Vaucouleurs profile), and b_n is an n -dependent normalization parameter ensuring that R_e encloses half the light. Typical star-forming galaxies (SFGs) are disk-dominated systems ($n \sim 1$) whereas quiescent galaxies (QGs) are bulge-dominated ($n \sim 4$). The correlation between galaxy structure and star formation activity appears to be established at least out to $z \sim 2.5$ (e.g., Wuyts et al. 2011a; Whitaker et al. 2015). Furthermore, central stellar mass surface density and bulge-to-total mass ratio are better correlated to specific star formation rate, color and fraction of quiescent galaxies than total stellar mass, suggesting that it is a good predictor of quiescence (Franx et al. 2008; Bell et al. 2012; Lang et al. 2014; van Dokkum et al. 2014). Given the result that massive disk QGs are rare, massive SFGs need to change their morphology from disk-dominated to bulge-dominated at some point and quench star formation around that time or soon thereafter.

On the other hand, it is also noted that the observed

correlation between galaxy structure and star formation activity does not necessarily imply physical causation. Lilly & Carollo (2016) demonstrate, using a simple toy model, that the correlation can naturally arise without any such physical role once the evolution of the size–mass relation for SFGs is taken into account (see also van Dokkum et al. 2015). It is important to determine how the structural evolution of the galaxy population proceeds by updating the knowledge about spatial distributions of stars and star formation in massive SFGs.

The effective radius of galaxies is another important parameter for understanding the morphological evolution. Many studies have shown that massive QGs at $z \sim 2$ are remarkably compact with $R_e \sim 1$ kpc, which is a factor of 4–5 smaller than the size of local QGs at fixed mass (e.g., Daddi et al. 2005; Trujillo et al. 2006; van Dokkum et al. 2008; van der Wel et al. 2014). Both simulations and observations support that massive compact QGs increase their size through gas-poor minor mergers (Bezanson et al. 2009; Naab et al. 2009; Newman et al. 2012; Williams et al. 2014). Massive compact SFGs have also been discovered at $z \sim 2$ and are naturally expected to be the direct progenitors of compact QGs (e.g., Barro et al. 2013; Nelson et al. 2014; Barro et al. 2014; Williams et al. 2014; Wisnioski et al. 2018). The evolutionary link from compact SFGs to compact QGs and eventually giant ellipticals has been extensively studied as mentioned above, while the evolutionary fate of extended SFGs has remained relatively less explored.

In the stellar mass range of $M_* < 10^{11} M_\odot$, the majority of SFGs at $z = 2$ have an extended disk with $R_e = 2 - 5$ kpc (e.g., Genzel et al. 2006; Law et al. 2012; van der Wel et al. 2014; Förster Schreiber et al. 2018) and form stars in the more extended disk (van Dokkum et al. 2015; Tacchella et al. 2015; Nelson et al. 2016b; Suzuki et al. 2019; Wilman et al. 2020). This inside-out growth scenario is also supported by a positive slope in the stellar mass–size relation (van der Wel et al. 2014). On the other hand, the inside-out growth alone can not fully explain the high Sérsic index ($n \sim 4$) in massive QGs or equivalently formation of a dense core. A combination of the inside-out growth and a declining star formation history can slightly increase the Sérsic index of massive SFGs from $n = 1$ to $n = 1.5 - 2$ (Lilly & Carollo 2016), but it is not enough. The question is how and when massive SFGs form a dense core and acquire a radial profile with $n \sim 4$.

To answer this question, we need to investigate where stars are formed in SFGs with stellar masses above $\log(M_*/M_\odot) = 11$, where morphological transformation and quenching are expected to occur (e.g., Bruce et al. 2012; Bell et al. 2012; Lang et al. 2014). The spatial distribution of stellar mass and ongoing star formation has been well studied over the past decade by observations of H α line and the rest-frame ultraviolet (UV) and optical continuum emission, as mentioned above. However, in this stellar mass range, 99% of the total star formation rate (SFR) is obscured by dust, and even H α emission misses 90%–95% of star formation (van Dokkum et al. 2015; Tadaki et al. 2017a; Whitaker et al. 2017). A radial gradient in dust extinction, furthermore, makes it difficult to study the spatial distribution of the total bolometric

star formation in massive SFGs using H α and UV (Nelson et al. 2016a; Tacchella et al. 2018).

Given that most star formation is obscured by dust, observing the spatially-resolved dust continuum is the best approach to determine where stars truly form in massive SFGs. For galaxies at $z \sim 2.2$, 870 μm observations sample the dust continuum emission in the rest-frame FIR ($\sim 270 \mu\text{m}$), corresponding to the Rayleigh–Jeans side of modified blackbody radiation with a dust temperature of 25 K. Total 870 μm flux densities are commonly used as a tracer of galaxy-integrated gas mass rather than infrared luminosity and SFR (Scoville et al. 2016) while it is reasonable to use the spatial distribution of 870 μm continuum emission to locate where the dusty star formation happens in galaxies. In this paper, we present *HST*-resolution observations of 870 μm continuum emission with the Atacama Large Millimeter/ submillimeter Array (ALMA) to study the spatial distribution of star formation in massive SFGs at $z = 2$. In Section 2, we describe the sample selection and ALMA observations. We show the results on detection rates of the 870 μm continuum emission and discuss the sample bias in Section 3. We measure the structural parameters of the dust emission through visibility fitting and compare the effective radius in the rest frame FIR with the effective radius in the optical in Section 4. Based on the size measurements both at FIR and optical, we discuss structural evolution and quenching in massive galaxies at $z = 2$ in Section 5. Finally, we give a summary in Section 6. We assume a Chabrier (2003) initial mass function (IMF) and adopt cosmological parameters of $H_0 = 70 \text{ km s}^{-1} \text{ Mpc}^{-1}$, $\Omega_M = 0.3$, and $\Omega_\Lambda = 0.7$.

2. SAMPLE AND OBSERVATIONS

2.1. Sample selection

We use the 3D-HST catalog including multi-wavelength photometry from ultraviolet to near-infrared and grism redshifts (Skelton et al. 2014; Momcheva et al. 2016) for 94,609 galaxies over 362 arcmin² of the UDS and GOODS-S fields in the CANDELS survey (Grogin et al. 2011; Koekemoer et al. 2011). Our sample selection for ALMA observations is as follows.

1. First, we consider a clean sample of galaxies with reliable photometry including *K*-band (O. Almaini et al. in preparation; Wuyts et al. 2008; Retzlaff et al. 2010) by adopting a flag of `use_phot=1` (see Skelton et al. 2014). This flag excludes stars, objects close to a bright star and galaxies whose photometric redshift is not derived.
2. Second, we select galaxies in the redshift range of $1.9 < z < 2.6$. The spectroscopic or grism redshift is used if available and otherwise the photometric redshift is used.
3. Third, we focus on the most massive galaxies with $\log(M_*/M_\odot) > 11$ in this work as this mass range is important for understanding the transformation of galaxy morphology, especially related to bulge formation (e.g., Bruce et al. 2012; Bell et al. 2012; Lang et al. 2014). Using the FAST code (Kriek et al. 2009), we perform spectral energy distribution (SED) fitting with stellar population synthesis models of Bruzual & Charlot (2003) under a

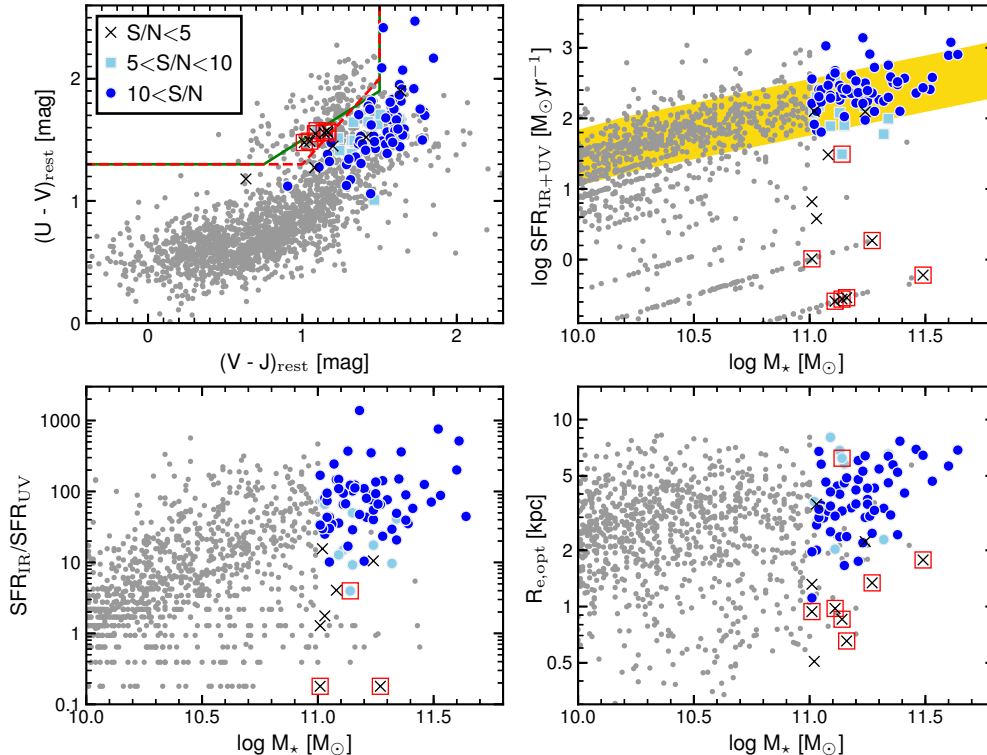


Figure 1. Top left: the rest-frame U-V vs. V-J color diagram for our ALMA sample of 85 massive SFGs at $z = 1.9 - 2.6$. Blue circles, light blue squares and black crosses indicate galaxies that are detected at above 10σ , at $5 - 10\sigma$ and not detected in the intermediate-resolution $870 \mu\text{m}$ images. Gray dots show all galaxies in the same redshift range, taken from the 3D-HST catalog (Skelton et al. 2014; Momcheva et al. 2016). A green continuous line shows the criteria to separate between star-forming and quiescent population, used in van Dokkum et al. (2015), while a red dashed line indicates our modified criteria, defined by Equation (4). Red open squares show 7 galaxies, which are classified as a quiescent population by the modified UVJ criteria. Top right: stellar mass vs. SFR. Our ALMA targets are mostly located within ± 0.4 dex of the star formation main sequence at $2 < z < 2.5$ (shaded region; a broken power law model in Whitaker et al. 2014). Bottom left: stellar mass vs. ratio of obscured to unobscured SFR. Bottom right: stellar mass vs. effective radius along the semi-major axis in the rest-frame optical (van der Wel et al. 2014).

Chabrier (2003) initial mass function and the dust attenuation law of Calzetti et al. (2000) to estimate stellar masses. We adopt exponentially declining star formation histories with reasonable constraints on the e -folding timescales and stellar ages (see also Wuyts et al. 2011b).

4. Finally, we apply the rest-frame UVJ color-color selection to separate SFGs from quiescent galaxies (e.g., Wuyts et al. 2007; Whitaker et al. 2011). 86 and 26 galaxies fall in the star-forming and the quiescent regime, respectively (Figure 1). Then, we select only UVJ -based SFGs.

We do not apply further selection criteria based on the SFR or optical morphology to ensure we have an unbiased sample of massive SFGs. One object (U4-5155) lies between two bright galaxies and is elongated with an effective radius of 5 arcsec in the $HST/F160W$ -band image (van der Wel et al. 2014). We exclude this galaxy from the sample as it is likely to be magnified by a gravitational lens. The final sample of 85 SFGs is listed in Table 1. 69 and 16 are located in UDS (191 arcmin^2) and GOODS-S field (171 arcmin^2), respectively. 19 are spectroscopically confirmed with the detection of the $H\alpha$ emission line in the KMOS^{3D} survey (Wisnioski et al. 2015, 2019) or the CO emission line by ALMA observations (Tadaki et al. 2017b). 32 have accurate red-

shifts ($\Delta z = \pm 0.02$) based on the HST grism spectra (Momcheva et al. 2016) or $H\alpha$ narrow-band imaging (Tadaki et al. 2013). For the remaining 34 galaxies, we use photometric redshifts. 12 and 3 targets overlap with the sample of Tadaki et al. (2017a) and Barro et al. (2016), respectively. We note that the 3D-HST catalog uses an $HST/F125W+F140W+F160W$ combined image for detection (Skelton et al. 2014), meaning they are effectively rest-optically selected. While the detection limit is much lower mass than $\log(M_{\star}/M_{\odot}) = 11$, it is possible that some unknown number of massive galaxies could be optically dark and missed (e.g., Franco et al. 2018; Yamaguchi et al. 2019). Currently, only several optically dark galaxies have been spectroscopically identified and they are all located at $z > 3$ (Pavesi et al. 2018; Wang et al. 2019; Williams et al. 2019; Umehata et al. 2020). This may be due to that the Balmer break at $z > 3$ is redshifted to be at the longer wavelength than the $HST/F160W$ -band, leading to non-detection in the HST images. Therefore, optically dark galaxies at $z \sim 2$ are likely to have lesser impact on the completeness of our sample.

2.2. Star formation activity

We estimate total SFRs by summing the rate of unobscured star formation measured from the rest-frame 2800 Å luminosities, corresponding to UV, and ob-

scured star formation from the total infrared (IR) luminosities following Kennicutt (1998), after conversion to a Chabrier (2003) IMF. We cross-match the 3D-HST, *Spitzer*/MIPS (24 μm) and *Herschel*/PACS (100 μm , 160 μm) catalogs built as described in Lutz et al. (2011) and Magnelli et al. (2013), with a maximum separation of 1.5". The IR luminosities are derived from the single band photometry at, in order of priority, 160 μm , 100 μm and 24 μm (Wuyts et al. 2011b). Three 160 μm -detected galaxies (U4-4706, U4-7472 and U4-36568) have a companion within 6" in the ALMA 870 μm images (see Section 2.4). We do not use their PACS photometry with a PSF size of FWHM=12" because it can be contaminated by the emission of the nearby 870 μm source. 44 and 32 are detected without contamination in the PACS and MIPS band, respectively. For the remaining 9 galaxies, we use the SFRs from SED fitting. Typical SFR uncertainties including systematic errors are ± 0.2 dex for IR-detected galaxies and ± 0.25 dex for the others (Wuyts et al. 2011b). In our ALMA sample, the ratio of obscured to unobscured SFR is, on average, $\text{SFR}_{\text{IR}}/\text{SFR}_{\text{UV}}=50$, indicating that the dust emission is a dominant probe of the star formation. Note that our sample is not biased toward a dusty population in the stellar mass range of $\log(M_*/M_\odot) > 11$, as shown in Figure 1.

As shown in Figure 1, most of our ALMA targets lie on/around the main sequence of star formation at $z \sim 2$ (Whitaker et al. 2014). The *UVJ* selection is useful for extracting SFGs without spectroscopic data while it would miss some objects with low-level star formation (e.g., Belli et al. 2017). 5 of 26 *UVJ*-selected QGs are detected in the PACS or MIPS band. It is not straightforward to estimate SFRs of QGs from the IR emission because the IR-based SFRs may be overestimated by contributions from evolved stellar populations (Utomo et al. 2014; Leja et al. 2019) or time-averaging effects for recently quenched galaxies (Hayward et al. 2014). The 5 QGs with IR detection are located near the bottom of the main sequence even if the IR emission is all originating from massive young stars. They are not included in our sample but it is going to have a minimal impact on our statistical analysis of a representative star-forming population.

2.3. Optical structure

Deep *HST*/WFC3 imaging data is available for our sample in the 3D-HST/CANDELS fields. Fitting of elliptical Sérsic models to the two-dimensional light profiles in the F160W-band image gives the structural parameters of the rest-frame optical emission: $R_{\text{e,opt}}$, n_{opt} , minor-to-major axis ratio q_{opt} , and position angle PA_{opt} (van der Wel et al. 2012, 2014; Lang et al. 2014). We adopt the effective radius along the semi-major axis to avoid inclination and projection effects, except for Section 5 where the circularized effective radius is used. We do not use 6 objects (U4-4706, U4-7472, U4-16795, U4-23044, GS4-2467 and GS4-5217) for optical size arguments because the best-fit Sérsic index reaches the constrained limit ($n = 0.2$ or $n = 8.0$) or the effective radius is unreasonably large with $R_{\text{e,opt}} > 1''$ (~ 10 kpc).

2.4. ALMA observations

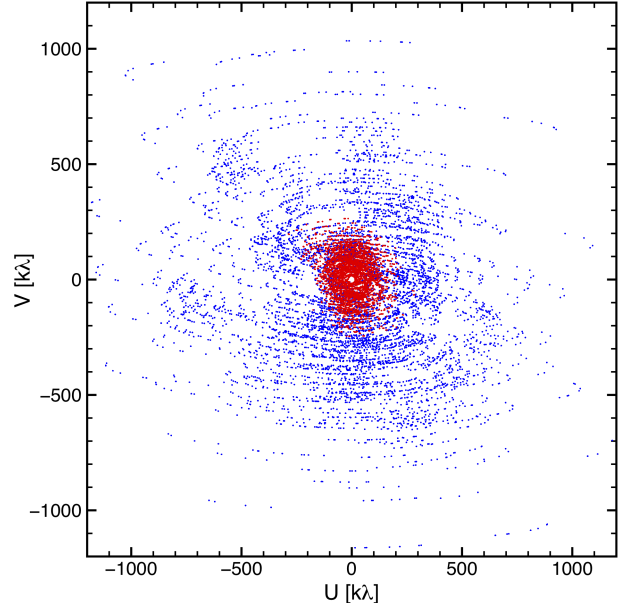


Figure 2. An example of the uv coverage in our ALMA observations (U4-190). The extended array data (blue) and the compact one (red) covers the uv range from 14 k λ to 1398 k λ and from 15 k λ to 349 k λ , respectively.

We have carried out ALMA observations of dust continuum emission in the mass-selected sample of SFGs at $z = 2$. We use the band 7 receivers with the 64-input correlator in Time Division Mode in a central frequency of 345 GHz (~ 870 μm). The frequency range available does not cover intermediate- J ($J_{\text{up}} < 7$) CO lines or atomic carbon lines at $z = 2$. We sample a wide range of spatial frequency in the uv plane by using two array configurations: compact array with baseline lengths of 15–300 m and extended array with 15–1260 m (Figure 2). The extended array data determine the spatial resolution of interferometric images produced through Fourier Transforms while the compact array data are crucial for measuring total fluxes, corresponding to visibility amplitudes in a zero baseline. If short baseline data were not sufficiently sensitive, the size measurements of 870 μm emission would be strongly biased by compact components in galaxies. The maximum recoverable scale of our ALMA observations is 6".7, corresponding to ~ 55 kpc at $z = 2$. We performed new observations of 84 galaxies with the compact array in May-June 2018 and 66 galaxies with the extended array in September 2018. The typical on-source time with 43–48 antennas is 4–5 minutes with the compact array and 7–9 minutes with the extended array. For the other galaxies in our sample, we use ALMA archival data (2012.1.00245.S, 2012.1.00983.S, 2013.1.00205.S, 2013.1.00566.S, 2013.1.00884.S, 2015.1.00242.S, 2016.1.01079.S) to avoid duplicate observations. We utilize the Common Astronomy Software Application package (CASA; McMullin et al. 2007) for the data calibration.

We create high-, intermediate-, and low-resolution images by changing the weights of visibilities. We clean images down to the 1.5σ level in a circular mask with a diameter of 2" (4" only for low-resolution images) using the CASA/*tclean* task. First, we create high-resolution images by using the compact array data with uv -distance

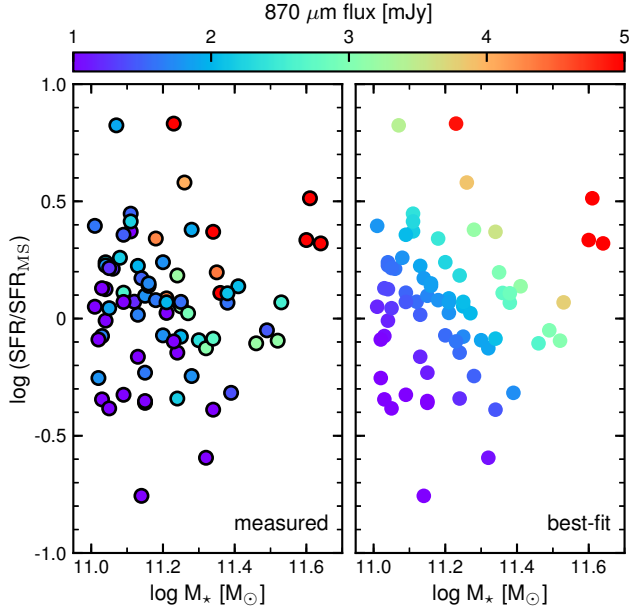


Figure 3. $870 \mu\text{m}$ flux densities for our ALMA sample of 74 galaxies at $S/N > 5$, as a function of stellar mass and offset in SFR from the main-sequence. Left: the peak flux densities measured in the low-resolution images. Right: the flux densities inferred from the stellar mass and SFR offset using Equation (2).

of $> 180 \text{ k}\lambda$ and all the extended array data and adopting a briggs weighting with a `robust` parameter of $+0.5$. The spatial resolution and the noise level is $0''.2\text{--}0''.3$ ($\sim 2 \text{ kpc}$) and $60 \pm 7 \mu\text{Jy}$, respectively. The high-resolution images are used only for visually inspecting the location and the morphology of the dust emission. Next, we create intermediate-resolution images by using all the compact array data and the extended array data with uv -distance of $< 180 \text{ k}\lambda$ and adopting `robust`= $+2.0$. The spatial resolution and the noise level is $0''.8\text{--}1''.0$ ($\sim 7 \text{ kpc}$) and $61 \pm 6 \mu\text{Jy}$, respectively. The intermediate-resolution images are useful for defining the signal-to-noise ratios (S/N) of $870 \mu\text{m}$ continuum emission while they are not sufficient for measuring the total fluxes from the whole galaxies. We therefore create low-resolution images from all the combined data with `uvtaper` = $4''$ and `robust`= 2.0 , resulting in the noise level of $174 \pm 29 \mu\text{Jy}$. The spatial resolution is $3''.3\text{--}3''.5$ ($\sim 28 \text{ kpc}$), which should cover whole galaxies at $z = 2$. Note that we do not primarily use these ALMA images for measuring the effective radius of $870 \mu\text{m}$ emission (section 4.1).

3. RESULTS

3.1. Detections of $870 \mu\text{m}$ continuum emission

We detect the $870 \mu\text{m}$ continuum emission from 74 of 85 galaxies at $S/N > 5$, 62 of which have $S/N > 10$, in the intermediate-resolution images. For 74 detected objects, we measure the total $870 \mu\text{m}$ flux density from the low-resolution images. As U4-7472 and U4-36568 have a companion $870 \mu\text{m}$ source within a radius of $1''.5$, we create low-resolution images after subtracting the companion in the visibility plane to measure the flux densities (section 4.1). The median flux density is $S_{\text{image}} = 1.8 \text{ mJy}$ in the range from 0.4 mJy to 6.9 mJy . Dust continuum emission on the Rayleigh–Jeans regime is commonly

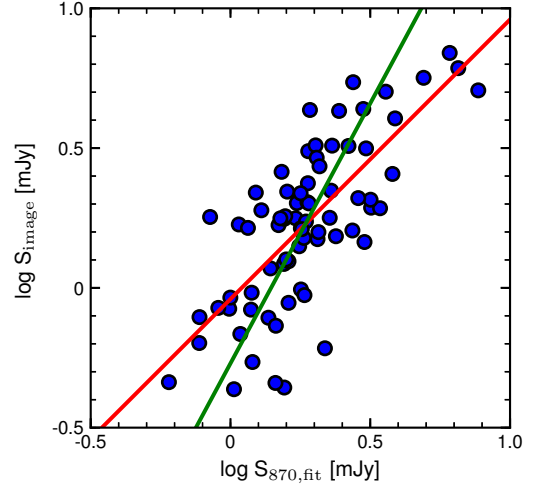


Figure 4. A comparison between the predicted and the measured flux densities for our ALMA sample of 74 galaxies at $S/N > 5$. A red line is the best-fit line ($S_{\text{image}} = 1.00 S_{870,\text{fit}} - 0.04$) from a least squares linear fit when the variable is $S_{870,\text{fit}}$. A green line is the best-fit line ($S_{\text{image}} = 1.86 S_{870,\text{fit}} - 0.27$) from a least squares linear fit when the variable is S_{image} .

used as a tracer of gas mass (e.g., Genzel et al. 2015; Scoville et al. 2016; Tacconi et al. 2018). We estimate gas mass in massive SFGs from the $870 \mu\text{m}$ flux density by using the calibration of Scoville et al. (2016). There is a clear trend of increasing flux density in the plane of stellar mass and offset of a galaxy from the star formation main sequence, SFR/SFR_{MS} , defined by a broken power law model in Whitaker et al. 2014. More massive, more actively star-forming galaxies are brighter at $870 \mu\text{m}$ (Figure 3). From a linear fitting in this parameter space, we derive equations to predict a $870 \mu\text{m}$ flux density and a gas mass of SFGs as,

$$\begin{aligned} \log S_{870,\text{fit}}[\text{mJy}] &= (0.95 \pm 0.15) \log M_* \\ &\quad + (0.52 \pm 0.08) \log\left(\frac{\text{SFR}}{\text{SFR}_{\text{MS}}}\right) \\ &\quad - (10.41 \pm 1.7), \end{aligned} \quad (2)$$

$$\begin{aligned} \log M_{\text{gas,fit}}[M_{\odot}] &= (0.95 \pm 0.15) \log M_* \\ &\quad + (0.53 \pm 0.08) \log\left(\frac{\text{SFR}}{\text{SFR}_{\text{MS}}}\right) \\ &\quad + (0.33 \pm 1.7). \end{aligned} \quad (3)$$

The dependence on SFR offset is identical to the general scaling relation covering the wide range of galaxy properties (Tacconi et al. 2018) while the mass-dependence is slightly stronger than in the scaling relation (exponent 0.67; Tacconi et al. 2018). The median and the standard deviation of the difference between the actual measurements and the best-fit values is $\log(S_{\text{image}}/S_{870,\text{fit}}) = -0.03 \pm 0.20 \text{ dex}$. On the other hand, there is a systematic error in the predictions by Equation (2): the flux densities are overestimated at $S_{\text{image}} < 1 \text{ mJy}$ and underestimated at $S_{\text{image}} > 3 \text{ mJy}$ (Figure 4). It is possible to correct for the systematics by applying $S_{870,\text{fit,cor}} = 1.86 S_{870,\text{fit}} - 0.27$, but the standard deviation of $\log(S_{\text{image}}/S_{870,\text{fit,cor}})$ increases to 0.27 dex . We also note that this prediction is valid only in the stellar mass

range of $\log(M_*/M_\odot) > 11$ and in the redshift range of $z = 1.9 - 2.6$.

In addition to the primary targets of massive SFGs at $z \sim 2$, we serendipitously detect 19 dust continuum sources at $S/N > 5.0$ in the regions within 13.6 arcsec of the phase center, where the primary beam correction factor is less than 0.15 (Table 2). The median redshift is $z = 2.7$ and the $870 \mu\text{m}$ flux density ranges from 0.4 mJy to 6.8 mJy after the primary beam correction. One source (U4-36568b) does not have an optical counterpart and is likely to be a massive SFG at $z > 3$ (e.g., Wang et al. 2019). 4 of 19 have a similar redshift to the primary targets with $|\Delta z| < 0.1$, suggesting that they are physically associated. In fact, one (GS4-44920 and GS4-45068) of the four pairs has been spectroscopically identified at $z = 2.448 - 2.450$ (Kurk et al. 2013), with a projected separation of $4'' (\sim 32 \text{ kpc})$.

3.2. Non-detected objects

For 11 non-detected objects, we give the 5σ upper limit of the $870 \mu\text{m}$ flux density from the low-resolution images. 6 of them are very close to the boundary of the quiescent regime in the UVJ diagram (van Dokkum et al. 2015) and have the lowest SFRs in our sample. Given that they lie about 2 dex below the main sequence at $z \sim 2$ in the M_* -SFR diagram (Figure 1), they are no longer representative of the star-forming population. Therefore, we use the modified UVJ criteria to define a clean sample of massive SFGs at $z \sim 2$ as,

$$\begin{aligned} V - J &< 1.5, \\ U - V &> 1.3, \\ U - V &> 1.4(V - J) - 0.1. \end{aligned} \quad (4)$$

The detection rate in the updated SFG sample increases from 87% to 94%, indicating it represents an almost mass-complete sample of SFGs down to $\log(M_*/M_\odot) = 11$.

For one galaxy (GS4-40185) classified as QGs in the modified criterion, we detect the $870 \mu\text{m}$ continuum emission at $S/N=5.5$. This galaxy is located below the main-sequence with $\log(\text{SFR}/\text{SFR}_{\text{MS}}) = -0.76$. The gas mass fraction is $M_{\text{gas}}/(M_* + M_{\text{gas}}) = 15\%$. This is more than twice smaller than the median value (37%) in 78 SFGs including 5 non-detected sources and is comparable to the gas fraction of a post-starburst galaxy at $z = 0.7$ (Suess et al. 2017). The less active star formation and the small gas fraction suggest that star formation is being quenched. Given that other 6 galaxies with similar quiescent UVJ colors are not detected at $870 \mu\text{m}$, GS4-40185 is a good candidate for studying the quenching mechanism, that probably works on a short timescale.

4. SIZE MEASUREMENTS OF $870 \mu\text{M}$ CONTINUUM EMISSION

4.1. Visibility fitting

Size measurements of dust emission usually require high S/N data. In analysis of images, the appearance and S/N depend largely on both the spatial resolution and the spatial extent of the dust emission. The spatial resolution is also coupled to the noise level since interferometers sample the Fourier transform of the intensity distribution within a finite uv coverage. Figure 5 shows

ALMA images of two galaxies with $S_{870} \sim 3 \text{ mJy}$, in which one is compact at $870 \mu\text{m}$ and the other is extended. As the compact object is detected at $S/N=29.7$ in the high-resolution image, it is possible to accurately measure the size by fitting Sérsic models to the image (Simpson et al. 2015a; Hodge et al. 2016; Gullberg et al. 2019). In contrast, the extended object is completely missed in the high-resolution image. One easy solution to measure the size is to use the intermediate-resolution image where the emission is detected at $S/N=17.1$, but inhomogeneous measurements lead to systematic uncertainties. The non-detection in the high-resolution image roughly means that the dust emission is extended and allows us to constrain the spatial extent. To fully utilize the information from observations, we measure the size of the $870 \mu\text{m}$ continuum emission by looking at how the visibility amplitudes change as a function of spatial frequency (Ikarashi et al. 2015; Simpson et al. 2015a; Tadaki et al. 2015). The visibility fitting in the uv plane provides homogeneous size measurements, regardless of the compact or extended nature of the sources analyzed (right panels of Figure 5).

To derive the structural parameters of the dust emission for 74 massive SFGs with $S/N > 5$ in our ALMA sample, we fit elliptical or circular Gaussian models to the observed data by using the UVMULTIFIT (Martí-Vidal et al. 2014). The details of the fitting process are described in Appendix A and the measured structural parameters are listed in Table 3. Only GS4-40185 ($S/N=5.5$) shows an extremely small size of $\text{FWHM} < 0''.01$, but this is probably due to the insufficient sensitivity as mentioned above. We use only 62 massive SFGs with $S/N > 10$ for discussion of the size measurements at $870 \mu\text{m}$.

In the GOODS-S field, we also find that there is a systematic offset of $\Delta\text{R.A.} = 0''.10$ and $\Delta\text{Dec.} = -0''.24$ in the central positions between *HST* and ALMA, which is reported in previous studies (Rujopakarn et al. 2016; Franco et al. 2018). In the UDS field, the systematic offset is small, $\Delta\text{R.A.} = 0''.08$ and $\Delta\text{Dec.} = -0''.06$. We correct for these offsets when the ALMA images are visually compared to the *HST* images (Figure 12).

Although most of the visibility data is well fitted by a Gaussian model, several objects show $> 1\sigma$ excesses over the model amplitude at small $u'v'$ and/or large $u'v'$ distances. The excess at both small and large $u'v'$ suggest a cuspy profile with an extended tail, corresponding to a higher Sérsic index ($n > 0.5$). Surface density profiles of stars and gas in star-forming galaxies are often characterized by an exponential function with $n = 1$ (Wuyts et al. 2011a; Hodge et al. 2016). We fit the visibility data to exponential disk models by fixing the axis ratio and the position angle to the values derived from Gaussian fitting. When adopting an exponential disk model, the measured fluxes and effective radii become on average larger by 5% and 3%, respectively.

4.2. Contributions of additional extended components

The visibility amplitudes at the zero baseline inferred from the best-fit models give a total flux density of galaxies. We compare the visibility-based flux densities for the Gaussian and exponential disk models with the peak flux densities measured in the low-resolution images (Figure 6). For $S/N > 10$ sources, the ratios of

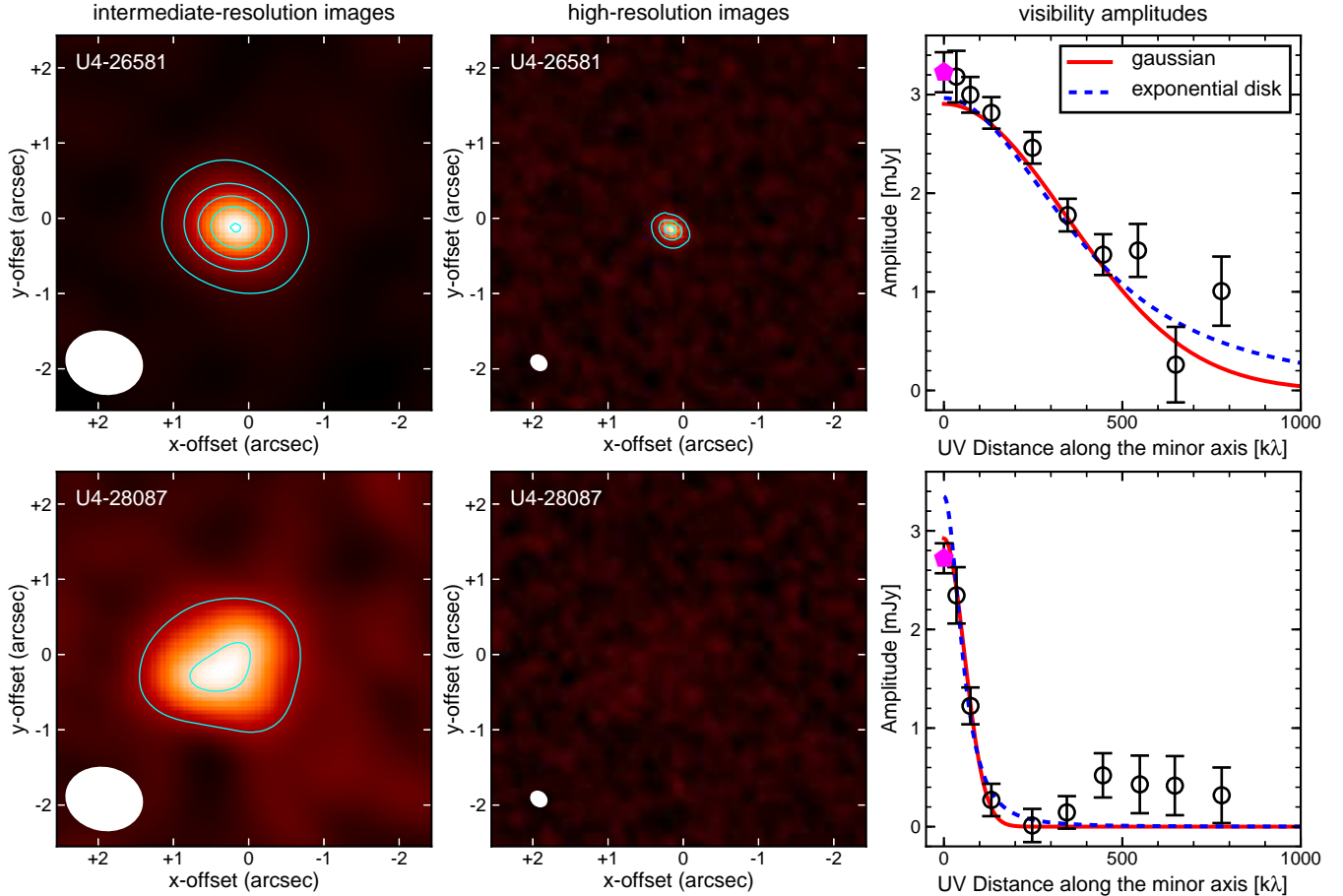


Figure 5. ALMA intermediate- and high-resolution images of the $870\ \mu\text{m}$ continuum emission from U4-26581 (top) and U4-28087 (bottom). The contours are plotted every 5σ in all images. Right panels show the visibility amplitudes as a function of uv distance along the minor axis, corresponding to the major axis in the images. Magenta pentagons show the peak flux density measured in the low-resolution images. Red solid lines and blue dashed lines indicate the best-fitting model for Gaussian and exponential profile, respectively. The fit was done to individual visibilities, not to the averaged ones shown by black circles in this figure.

the difference between visibility-based and image-based flux densities are on average $S_{\text{visibility}}/S_{\text{image}} = 0.93$ in the Gaussian and $S_{\text{visibility}}/S_{\text{image}} = 0.98$ in the disk model, indicating that the dust emission is better characterized by an exponential profile (Hodge et al. 2016; Gullberg et al. 2019). We therefore use the effective radius from the disk model in the subsequent sections. In the disk model, compact objects with $R_{\text{e,FIR}} < 0''.125$ show more deficiency of the visibility-based flux densities with $S_{\text{visibility}}/S_{\text{image}} = 0.88$. Especially for two compact objects (U4-34138 and U4-34617), the best-fit visibility model includes only 50–70% of the total flux densities measured in the low-resolution images. They may have additional components such as an extended halo, off-center clumps or an active galactic nucleus (AGN) or be building cuspy bulges.

For extended objects with $R_{\text{e,FIR}} > 0''.125$, the visibility-based flux densities are in good agreement with the image-based one, with $S_{\text{visibility}}/S_{\text{image}} = 1.01$. To evaluate the contributions of additional components, we perform a stacking analysis of the model-subtracted visibilities for subsamples of 13 compact objects (excluding U4-34138 and U4-34617) and 47 extended objects, using the STACKER tool (Lindroos et al. 2015). The phase center is individually shifted to the center position of

the best-fit model before the stacking. We then create low-resolution images from the stacked visibility with $\text{uvtaper} = 4''$ and $\text{robust} = 2.0$, resulting in $3''.4$ resolution. The tapered images can in principle recover extended emission even with $R_{\text{e,FIR}} = 0''.5$ (Gullberg et al. 2019). To demonstrate it, we make simulations, which add a Gaussian component with a different flux density to the stacked visibilities and measure the peak flux density in the tapered images. The source size is assumed to be $R_{\text{e,FIR}} = 0''.5$. Then, we find that one can recover almost 100% of the extended emission in the tapered images.

For our ALMA sample, the residual emission we have detected in the tapered images has $220 \pm 57\ \mu\text{Jy}$ (3.8σ) for compact objects and $80 \pm 26\ \mu\text{Jy}$ (3.1σ) for extended objects. The contribution to the total flux density is 11% (4–21%) for compact objects and 4% (1–10%) for extended objects. We also numerically calculate the effective radius with taking into account the extended component by assuming 2 component models, which consist of the best-fit disk model and an extended gaussian with the stacked flux densities. Then, we find that the extended component would change the effective radius by 13% (4–29%) for compact objects and by 4% (1–11%) for extended objects. Therefore, the residual emission

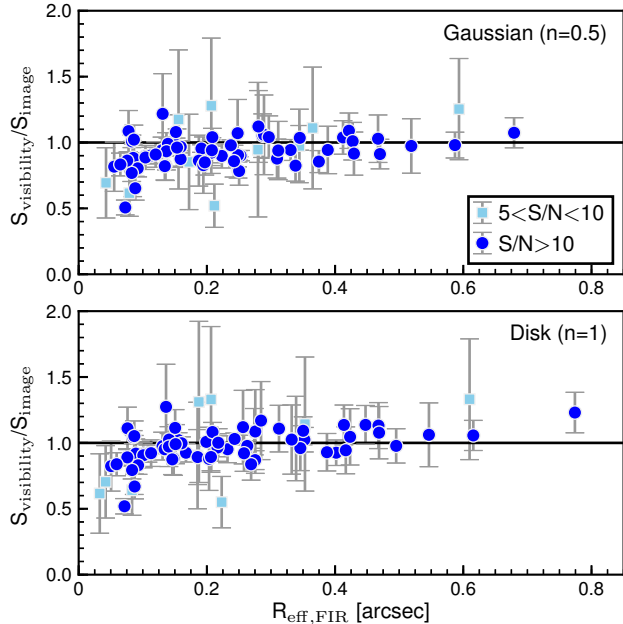


Figure 6. Comparisons between visibility-based and image-based flux densities in the low-resolution images as a function of the effective radius of $870\ \mu\text{m}$ emission. The visibility-based flux densities and sizes are derived from the best-fit model with Gaussian (top) and exponential profile (bottom). Blue circles and light blue squares indicate galaxies that are detected at above 10σ and at $5-10\sigma$ in the ALMA intermediate-resolution images, respectively.

including an extended component has less impact on the measurements of the effective radius, except for U4-34138 and U4-34617.

4.3. Comparison with submillimeter bright galaxies

We compare the $870\ \mu\text{m}$ properties of massive SFGs at $z = 2$ with those of submillimeter bright galaxies (SMGs) at $z = 1-4$ (Gullberg et al. 2019). The SMG sample is originally detected as 716 single-dish $850\ \mu\text{m}$ sources with flux densities of $S_{850} > 3.4\ \text{mJy}$ by JCMT survey (Geach et al. 2017) and is identified as 706 galaxies by ALMA followup observations (AS2UDS; Stach et al. 2019). 153 of 706 SMGs have robust size measurements from ALMA $0''.18$ -resolution observations (Gullberg et al. 2019). Our mass-selected sample of SFGs has a median flux density of $1.8\ \text{mJy}$, which is three times fainter than the flux-limited sample of SMGs. As shown in Figure 7, massive SFGs are distributed over a wide range of the FIR size from $R_{\text{e,FIR}} = 0''.05$ to $R_{\text{e,FIR}} = 0''.8$ while SMGs are mostly compact with $R_{\text{e,FIR}} < 0''.2$. Other 354 objects in the SMG sample are detected in the same ALMA observations, but their size was not measured due to the low S/N of < 8 . The subsample of 153 SMGs is potentially biased to a compact population because the low S/N can be partly caused by extended dust emission as well as faint emission.

On the other hand, the observational bias alone is unlikely to be responsible for the size difference between the two samples. Even in our ALMA sample, we find that none of 10 bright sources with $S_{870} > 3.4\ \text{mJy}$ are extended with $R_{\text{e,FIR}} > 0''.3$ while 33% of the fainter sources are extended. We also evaluate the completeness in our ALMA observations from the CASA simulations. Although some faint and extended emission can be missed

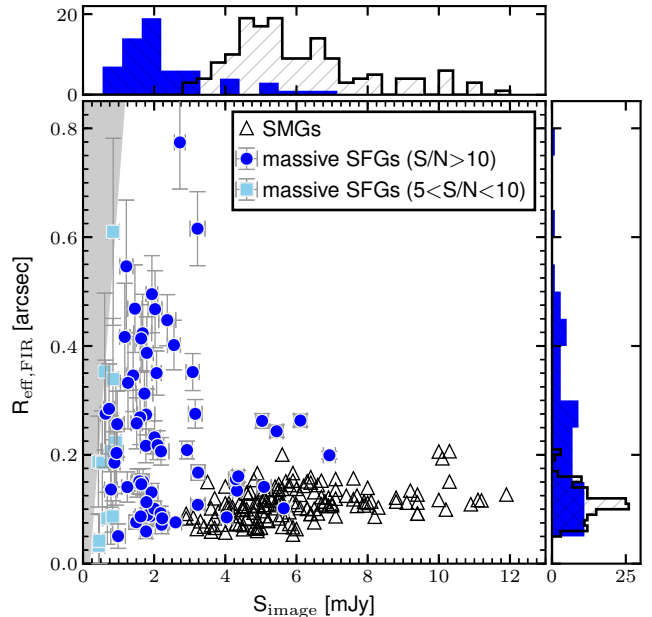


Figure 7. $870\ \mu\text{m}$ flux densities and effective radius in massive SFGs at $z = 2$ (blue circles and light blue squares) and SMGs at $z = 1-4$ (open triangles; Gullberg et al. 2019). A gray-shaded region shows faint and extended emission that can not be detected at above 5σ in the simulated observations (Appendix B). The histogram in the top and right panel is the projected distributions of $870\ \mu\text{m}$ flux densities and effective radius for massive SFGs (filled blue) and SMGs (open black).

in our observations, the incompleteness effect is negligible especially at $S_{870} > 1\ \text{mJy}$ (a shaded region in Figure 7). This result confirms the previous results that the bright emission in SMGs originates in their compact core with a high surface density of dust, not in a large disk (Gullberg et al. 2019). Some physical mechanism that forces a large amount of gas into the central region of galaxies is likely to be at work, causing the compact starburst.

4.4. Comparison of the rest-frame optical and far-infrared size

Overlay images illustrate that the dust continuum emission is centrally-concentrated while the rest-frame optical emission appears to be extended in the *HST*/F160W-band images (Figure 12 and Figure 13 in Appendix A). As the *HST*/F160W-band traces emission in the rest-frame wavelength between *B*-band and *V*-band at $z = 1.9-2.6$, it is still affected by dust extinction. A heavily obscured region does not become bright in the *HST* images while it is very bright in the ALMA images. The ALMA images are not sensitive to low-level, unobscured star formation such as off-center blue clumps (e.g., Wuyts et al. 2012). Nevertheless, dust continuum emission can serve as a primary probe of the spatial distribution of the total star formation in massive SFGs because more than 95% of the star formation is obscured by dust in the stellar mass range of $\log(M_*/M_\odot) > 11$ (Figure 1).

4 of 62 massive SFGs with $S/N > 10$ do not have robust size measurements in the *HST*/F160W-band (Section 2.3). For the remaining 58 massive SFGs in our ALMA sample, the effective radius in

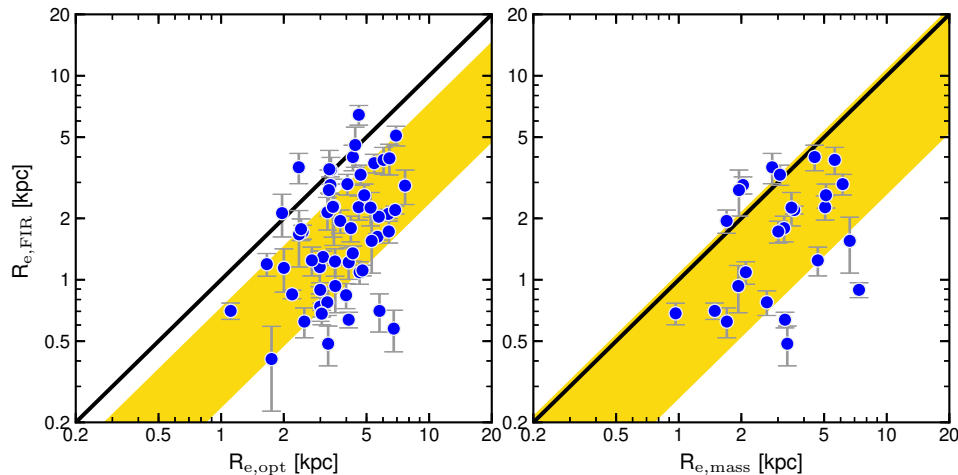


Figure 8. Size comparisons between the rest-frame FIR, optical and the stellar mass distribution. Yellow-shaded regions show the 16th and 84th percentiles of the size ratios, $R_{e,opt}/R_{e,FIR} = 2.3^{+1.9}_{-1.0}$ and $R_{e,mass}/R_{e,FIR} = 1.9^{+1.9}_{-1.0}$.

the FIR is smaller by a factor of $2.3^{+1.9}_{-1.0}$ than that in the optical, placing results from previous studies on a more robust footing (Simpson et al. 2015b; Barro et al. 2016; Rujopakarn et al. 2016; Tadaki et al. 2017a; Calistro Rivera et al. 2018; Elbaz et al. 2018; Fujimoto et al. 2018; Nelson et al. 2019; Lang et al. 2019; Chen et al. 2020). The above range is based on the 16th and 84th percentiles of the optical-to-FIR effective radius ratio. The optical light distribution is commonly used as a probe of stellar mass distribution. However, the half-light radius is expected to be larger than the half-mass radius especially for old or dusty galaxies where there is a strong radial dependence of mass-to-light ratio (e.g., Mosleh et al. 2017; Price et al. 2017; Suess et al. 2019).

For galaxies in the 3D-HST/CANDELS fields, Lang et al. (2014) have constructed a mass-to-light ratio map in the *HST*/F160W-band through the resolved SED modeling with the multiband HST data (Wuyts et al. 2012) and created a stellar mass map from the *HST*/F160W-band map without decreasing the spatial resolution. Then, they have fitted single Sérsic models to the stellar mass map to derive the half-mass radius. For our sample, 26 of 58 massive SFGs have measurements of the half-mass radius from Lang et al. (2014). The typical uncertainty on the half-mass radius is $\sim 10\%$ for dusty SFGs (Lang et al. 2019). Other galaxies are excluded because the best-fit Sérsic index reaches the constrained limit ($n = 0.2$ or $n = 8.0$) or the effective radius is unreasonably small with $R_{e,mass} < 0''.05$. The ratio of the half-mass to the half-light radius is $R_{e,mass}/R_{e,opt} = 0.8^{+0.5}_{-0.3}$, which can be interpreted as that the optical continuum emission is indeed affected by strong dust extinction in the center of galaxies. However, the effective radius in the FIR is still by a factor of $1.9^{+1.9}_{-0.9}$ smaller than the half-mass radius (Figure 8). These results suggest that many massive SFGs intensively form stars in a compact central region, embedded in a more extended disk probed by the optical continuum emission.

We also compare the FIR size with the $H\alpha$ size. 8 of 58 massive SFGs have measurements of the effective radius of the $H\alpha$ emission from the KMOS^{3D} survey

(Wisnioski et al. 2019; Wilman et al. 2020). The median ratio between the $H\alpha$ and the FIR effective radius is $R_{e,H\alpha}/R_{e,FIR} = 2.3$ though both trace star formation. The more heavily obscured regions is unlikely to be probed by the rest-frame UV and $H\alpha$ emission (Chen et al. 2020).

We caution that conversion from $870 \mu\text{m}$ flux to dust-obscured SFR depends on dust properties such as dust temperature and optical depth. When dust temperature is higher in a galaxy center, the spatial distribution of infrared luminosity becomes more compact than that of dust continuum emission. In contrast, the spatial distribution of dust mass becomes more extended than that of dust continuum emission. This can explain the result from previous studies that the effective radius of intermediate- J ($J_{\text{up}} = 3$ and 4) CO emission is larger than that of dust continuum emission in massive SFGs and SMGs (Chen et al. 2017; Tadaki et al. 2017b; Calistro Rivera et al. 2018; Tadaki et al. 2019). Simulations also show that the spatial distribution of dust emission is more compact than the total gas component, but has a similar spatial distribution as the cold, dense gas (Cochrane et al. 2019). An optical depth effect on dust continuum emission could also lead to a smaller size of star formation because emission at shorter wavelengths (tracing an infrared luminosity) is preferentially suppressed in a galaxy center. Therefore, the distribution of dust-obscured SFR could be even more compact than measured from the $870 \mu\text{m}$ continuum observations, supporting our result that massive SFGs form stars in a compact region.

4.5. Correlations between the size ratio and other galaxy parameters

In the previous section, we found that the effective radius of the FIR emission is smaller than that of the optical emission in massive SFGs. We investigate how the optical-to-FIR effective radius ratio is correlated with other galaxy parameters, including redshift, stellar mass, Sérsic index in the optical, dust extinction A_V , offset from the star formation main-sequence, and gas mass fraction (Figure 9). Then, we compute the Spearman rank correlation coefficient and the p -value to test for

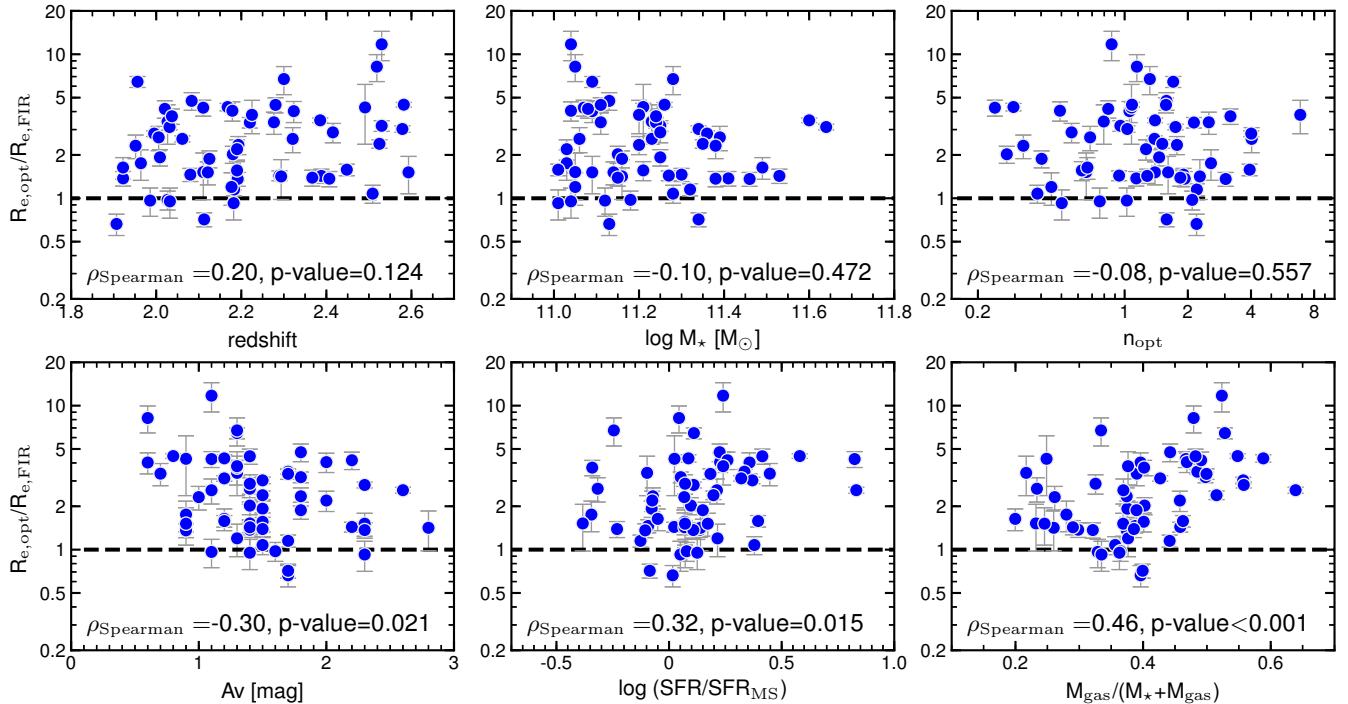


Figure 9. Optical-to-FIR effective radius ratio vs. redshift (top left), stellar mass (top center), Sérsic index (top right), dust extinction (bottom left), offset from the star formation main-sequence (bottom center), and gas mass fraction (bottom right).

non-correlation. When the p -value is very close to 0, we can reject the null hypothesis that the observed correlation is zero. In regard to the redshift, stellar mass, and Sérsic index, there is no significant correlation with the size ratio. The optical-to-FIR effective radius ratio is weakly anticorrelated with the dust extinction, derived from SED fitting to the galaxy-integrated photometry from the rest-frame UV to near-IR, probed by observed optical to mid-IR fluxes. This is the opposite of what is expected because strong dust extinction in galaxy centers can make the optical effective radius larger. At least, we do not find evidence that the optical-to-FIR effective radius ratio is larger due to dust extinction. Also, the ratio is positively correlated with the gas mass fraction and the offset from the star formation main-sequence. The Spearman rank correlation coefficient and the p -value is $\rho_{\text{Spearman}} = 0.46$ and $p < 0.001$ for gas mass fraction and $\rho_{\text{Spearman}} = 0.32$ and $p = 0.015$ for main-sequence offset, respectively.

The more centrally-concentrated star formation than stars indicates that gas is transported from the outer disk into the galaxy center. The fact that more gas-rich, more actively star-forming galaxies tend to have larger $R_{e,\text{opt}}/R_{e,\text{FIR}}$ suggests the possibility that the more compact dust emission is related to dissipative processes such as wet compaction. A dissipative concentration of gas (*wet compaction*) is seen in simulations of gas-rich galaxies at high-redshift (e.g., Noguchi 1999; Immeli et al. 2004; Bournaud et al. 2014; Zolotov et al. 2015; Tacchella et al. 2016). Wet compaction is triggered by gas-rich minor/major mergers, counter-rotating streams, and radial gas inflows driven by violent disk instability (e.g., Dekel & Burkert 2014; Forbes et al. 2014). There is also observational evidence of a gas component falling into an SMG with a compact core from a di-

rection perpendicular to the disk rotation (Tadaki et al. 2020). The onset of wet compaction is likely to occur when gas inflows dominate star formation and outflows (Tacchella et al. 2016). It is therefore expected that the incidence of compaction depends on star-forming activity and gas mass fraction in galaxies. When gas falls into the galaxy center to feed a core, it has to lose angular momentum. The extended H α disk (section 4.4) may be formed by the released angular momentum.

5. DISCUSSION

Since we derive the spatial distribution of stellar continuum emission from the *HST*/F160W data and the distribution of dusty star formation from the ALMA data, we combine the two to predict how massive SFGs will change their effective radius and their central stellar mass within a radius of 1kpc, $M_{1\text{kpc}}$, by in-situ star formation. We discuss the current and future structure for 58 massive SFGs with robust measurements of the structural parameters in both *HST*/F160W and ALMA data. Unlike the previous sections, we adopt the circularized effective radii of the optical and the FIR emission to treat them fairly since the axis ratios and the position angles are not exactly the same.

5.1. Spatially-resolved stellar mass and SFR

Before investigating the structural evolution of massive SFGs at $z \sim 2$, we look at their spatially-resolved stellar mass and SFR at the observed epoch. The surface stellar mass profile and the surface SFR profile are derived from the best-fitting Sérsic profile in the *HST*/F160W and ALMA/870 μm data, respectively. Following previous studies (Bezanson et al. 2009; Mowla et al. 2019), we deproject the two-dimensional Sérsic profile using an Abel transform (see also Appendix C). We scale the integral

of the inferred three-dimensional profile at *HST*/F160W to the total stellar mass and that at ALMA 870 μm to the total SFR to compute the central mass ($M_{1\text{kpc}}$) and the central SFR within a radius of 1kpc ($\text{SFR}_{1\text{kpc}}$). Once the central mass and SFR are given, it is possible to estimate the stellar mass and SFR in the outer disk with $R > 1$ kpc by subtracting $M_{1\text{kpc}}$ and $\text{SFR}_{1\text{kpc}}$ from the total stellar mass and the total SFR.

Figure 10 shows a spatially-resolved version of the mass–SFR plane for our ALMA sample. The outer disks are responsible for the total stellar mass while the SFR in the central 1kpc regions is comparable to that in the outer disks. This leads to a significant difference in the star formation activity. About half of the central 1kpc regions are located above the star forming main-sequence defined by galaxy-integrated properties while the outer disks mostly lie on the main-sequence. The median value and the standard deviation of the specific SFRs, defined as $\text{sSFR} = \text{SFR}/M_*$, is $\log \text{sSFR} [\text{Gyr}^{-1}] = 0.83 \pm 0.71$ for the central 1kpc region and $\log \text{sSFR} [\text{Gyr}^{-1}] = 0.04 \pm 0.33$ for the outer disk, indicating that the sSFR is higher in the galaxy center than in the outer disk.

The centrally-rising sSFR profiles seem to be at odds with previous studies that have applied dust gradient corrections to translate $\text{H}\alpha$ profiles to SFR profiles, finding that dust-corrected sSFR profiles are centrally dipping in massive SFGs at $z \sim 2$ (Tacchella et al. 2015, 2018; Suzuki et al. 2019). This difference may be due to underestimates of the central dust extinction and/or the different sample selection. Nelson et al. (2016a) find significant dust attenuation toward centers of massive SFGs through the Balmer decrement although it is not very deep into dust-embedded regions as can be probed by FIR emission. In our ALMA observations, it was difficult to derive the spatial distributions of star formation for less dusty SFGs near the bottom of the star-forming main sequence, corresponding to $\text{S/N} < 10$ sources. As shown by Tacchella et al. (2018), massive less dusty SFGs are likely to have centrally-dipping sSFR profiles. Dust extinction corrections based on the rest-frame UV color, as applied by Tacchella et al. (2018), may be prone to saturation effects in the case of a mixture between obscuring dust clouds and the emitting sources. Also, many of massive SFGs are very faint and fuzzy in the *HST*/F814W-band images, making it difficult to determine the rest-frame UV color at $z \sim 2$ in the first place. Therefore, it would be necessary to use the appropriate indicators, depending on the galaxy properties: submillimeter continuum for massive, dusty SFGs on/around the star-forming main sequence and $\text{H}\alpha$ line emission for less dusty SFGs.

5.2. Structural evolution in massive star-forming galaxies

Next, we investigate the time evolution of the effective radius and the central mass assuming that the current level of star formation and its spatial distribution are the same for several hundred megayears. The mass of newly formed stars is estimated to be

$$M_{*,\text{new}} = \text{SFR} \times \tau_{\text{SF}} \times \beta \quad (5)$$

where τ_{SF} is the timescale for star formation and β is the mass loss parameter due to supernova explosions

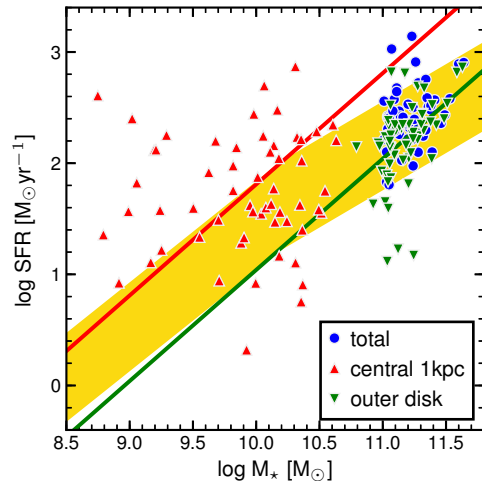


Figure 10. The stellar mass vs. SFR for the central 1 kpc regions (red triangles) and the outer disks (green triangles) of massive SFGs. Red and green lines correspond to the median sSFR for the central 1 kpc regions ($\log \text{sSFR} [\text{Gyr}^{-1}] = 0.83$) and the outer disks ($\log \text{sSFR} [\text{Gyr}^{-1}] = 0.04$), respectively. A yellow shaded region shows the ± 0.4 dex range of the star formation main sequence at $2 < z < 2.5$ (Whitaker et al. 2014). We also show the total stellar mass and total SFR by blue circles.

and stellar winds. We adopt $\beta = 0.6$ appropriate for a Chabrier (2003) IMF. Figure 11 shows the circularized effective radius and the central mass inside a radius of 1 kpc as a function of stellar mass at $\tau_{\text{SF}} = 0$ Myr, 300 Myr and 600 Myr. We overplot the 16th and 84th percentiles in each mass bin for SFGs and QGs at $z = 1.9 - 2.6$ in the combined sample of the CANDELS/3D-HST survey (van der Wel et al. 2014; Skelton et al. 2014; Momcheva et al. 2016) and the COSMOS-DASH survey (Mowla et al. 2019).

We find that by 300 Myr with the compact starburst, most of massive SFGs lie on the mass-size relation for QGs (Figure 11). This is one of the most important results of this work. In our ALMA sample of 58 massive SFGs, the effective radius is decreased, on average, by 14% in 300 Myr while the stellar mass is increased by 28%. The averaged evolution in the mass-size plane is approximated by $\Delta \log R_e = -0.6 \Delta \log M_*$. The negative slope appears to contradict the context of inside-out growth where galaxies form stars in a more extended disk and gradually increase their size with $\Delta \log R_e \sim 0.3 \Delta \log M_*$ (van Dokkum et al. 2015). Our result is preferred for explaining the morphological transformation of massive SFGs, at least in terms of effective radius.

We also infer the effective radius of the massive SFGs at higher redshift by putting $\tau_{\text{SF}} = -300$ Myr in Equation (5). Many of them are found to deviate from the observed mass-size relation and become too large especially in the stellar mass range of $\log(M_*/M_\odot) < 11$, suggesting that very little time has passed since the compact starburst occurred. Extended star formation in disks is required for explaining the size evolution of SFGs, but it does not transform the morphology of galaxies from disk-dominated to bulge-dominated. The compact starburst naturally produces a cuspy profile, characterized by a high Sérsic index. This outside-in transformation should happen after the inside-out growth of galaxy

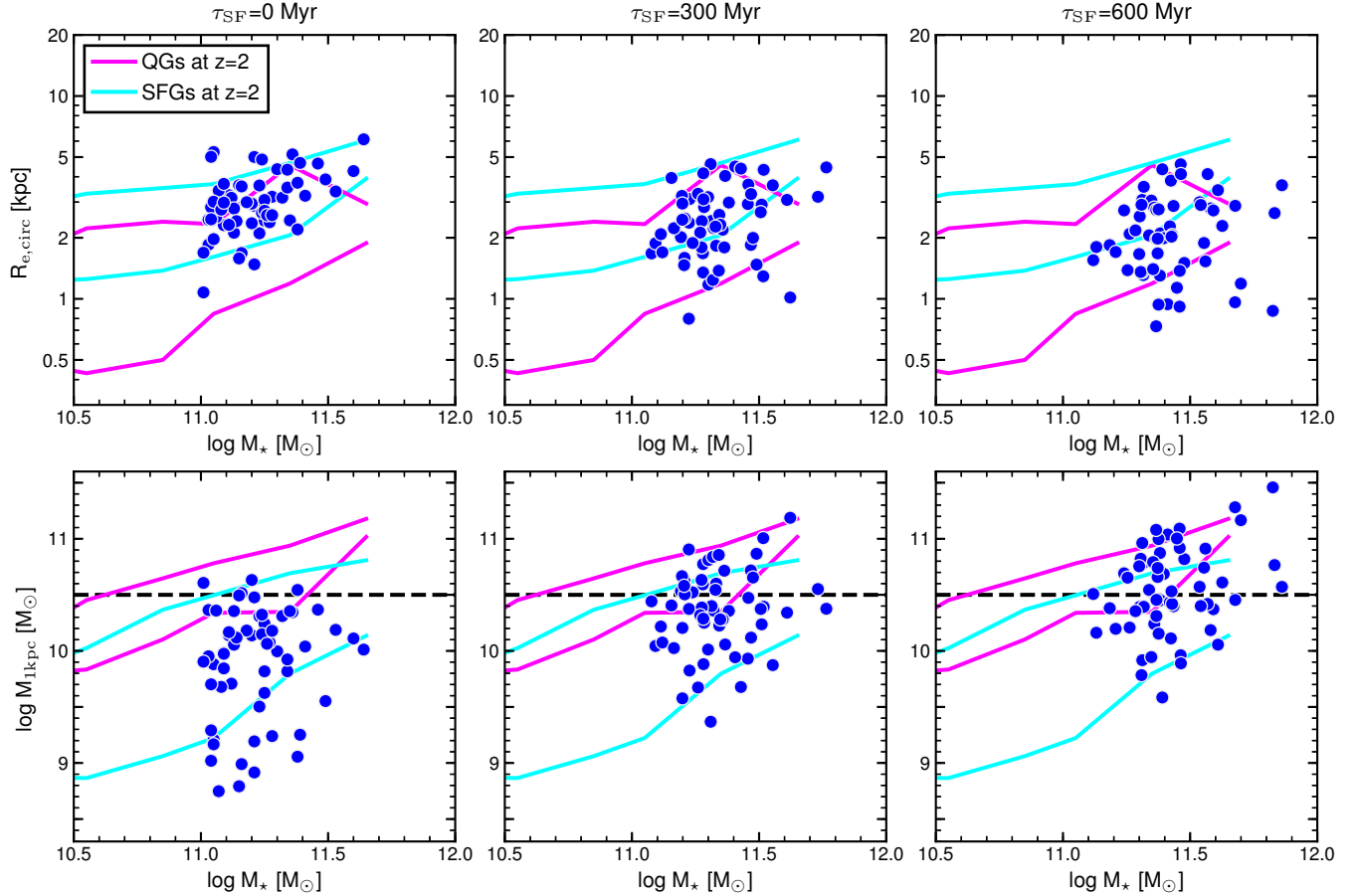


Figure 11. The effective radius of the optical emission (top) and the central 1 kpc mass (bottom) as a function of stellar mass for 58 massive SFGs in our ALMA sample. We show the observed values at $\tau_{\text{SF}} = 0$ (left) and the inferred values at $\tau_{\text{SF}} = 300$ Myr (center) and $\tau_{\text{SF}} = 600$ Myr (right), which are based on the spatial distribution of the $870 \mu\text{m}$ continuum emission (Section 5.2). Cyan and magenta lines indicate the 16th and 84th percentiles in each bin of stellar mass for SFGs and QGs at $z = 1.9 - 2.6$ in the combined sample of the CANDELS/3D-HST survey (van der Wel et al. 2014; Skelton et al. 2014; Momcheva et al. 2016) and the COSMOS-DASH survey (Mowla et al. 2019). Black dashed lines indicate $\log(M_{1\text{kpc}}/M_{\odot}) = 10.5$, which defines a dense core in this work.

disks. Observations of massive, $\log(M_{\star}/M_{\odot}) > 11$, early-type galaxies at $z \sim 0$ show that the mass-weighted age in the galaxy center is younger than that in the outer disks (Goddard et al. 2017), supporting the outside-in transformation.

On the other hand, the fact that going 300 Myr back in time brings many galaxies outside the mass-size relation suggests not only that the compact starburst can not have been going on for a long time, but also that it will not go on for a long time after the current time of the observations either. As it is implausible to find all observed systems in the first fraction of their compact starburst phase, it may not be reasonable to extrapolate the current distributions of star formation into the future beyond 300 Myr. This is also supported by the result that some of massive SFGs become more compact, $R_e < 1$ kpc, than massive QGs at $\tau_{\text{SF}} = 600$ Myr.

Based on the current distribution of star formation, we also find that 22 ($\sim 38\%$) of 58 massive SFGs have a dense core with $\log(M_{1\text{kpc}}/M_{\odot}) > 10.5$ at $\tau_{\text{SF}} = 300$ Myr and additional 8 (a total of 30, $\sim 52\%$) reach this threshold at $\tau_{\text{SF}} = 600$ Myr. Further star formation will allow the remaining SFGs to form a dense core in about 2 Gyr, but it is unlikely to happen as mentioned

above. The compact starburst probed by ALMA observations makes $\sim 40\%$ of massive SFGs form a dense core with $\log(M_{1\text{kpc}}/M_{\odot}) > 10.5$ whereas $\sim 75\%$ of massive QGs with $\log(M_{\star}/M_{\odot}) > 11$ reach this threshold (Figure 11). Despite the fact that most of our sample has highly compact dust emission, more than a half of massive SFGs do not form enough stars in this episode to reach the central mass density of $\log(M_{1\text{kpc}}/M_{\odot}) > 10.5$. They need to make their distribution of star formation more compact to form a dense core if galaxies transform their morphology before quenching. An alternative view is that massive SFGs evolve into disk QGs without a dense core, although measurements of Sérsic index indicate that such cases are infrequent (e.g., Wuyts et al. 2011a; Whitaker et al. 2015). Recent studies have found that three gravitationally lensed QGs at $z \sim 2$ are rotationally supported and one of them has a perfect exponential disk with no evidence for a dense core (Toft et al. 2017; Newman et al. 2018a,b). Some of massive SFGs may be the immediate progenitors of disk QGs at $z \sim 2$, but it could be a minor pathway as indicated by the fact that 75% of massive QGs have a dense core.

Using ALMA, we have made high-resolution observations of 870 μm continuum emission for the mass-selected sample of 85 massive, $\log(M_*/M_\odot) > 11$, SFGs at $z = 1.9 - 2.6$ in the CANDELS/3D-HST fields of UDS and GOODS-S. We have detected the dust continuum emission from 74 galaxies and robustly measured the effective radius for 62 galaxies. 58 of them have robust size measurements in the *HST*/F160W band. Combining the distribution of star formation from the ALMA data with that of stellar continuum from the *HST* data, we have investigated the structural evolution in massive SFGs at $z = 2$.

1. The 870 μm flux density ranges from 0.4 mJy to 6.9 mJy and increases as a function of stellar mass and offset from the star-forming main sequence. As the gas mass can be estimated from the 870 μm flux density, we confirmed the trend that more massive, more active SFGs have a larger gas reservoir. 6 of 11 non-detected sources are located near the boundary between star-forming and quiescent population in the *UVJ* diagram. Once we adopt the slightly modified boundary, the detection rate is 94% (73/78), indicating that our targets represent a nearly mass-complete sample of SFGs.
2. The effective radius of the 870 μm emission widely ranges from 0.4 kpc to 6 kpc. Many massive SFGs are more extended in the FIR than bright SMGs with $S_{870} > 3.4$ mJy at $z = 1 - 4$. The significant difference of the FIR size between the mass-selected and the flux-selected sample can be partly caused by the observational bias, where high-resolution ALMA images are not sensitive to extended emission. On the other hand, there is a lack of bright extended sources with $S_{870} > 3.4$ mJy and $R_{e,\text{FIR}} > 0''.3$ even in our ALMA sample of massive SFGs, indicating that the bright submillimeter emission originates in not their large disk but their compact core.
3. The effective radius in the FIR is smaller by a factor of $2.3_{-1.0}^{+1.9}$ than the effective radius in the optical and smaller by a factor of $1.9_{-1.0}^{+1.9}$ than the half-mass radius. The compact dust emission suggests that many massive SFGs intensively form stars in the central 1 kpc region, embedded in a more extended disk probed by the optical continuum emission.
4. We found that the FIR size is weakly anticorrelated with the gas mass fraction: gas-rich galaxies tend to be associated with compact dust emission. This evidence is consistent with dissipative concentration of gas towards the center of gas-rich galaxies via efficient radial inflows
5. We derive the stellar masses and the SFRs separately in the central 1 kpc region and in the outer disk by exploiting the best-fit Sérsic profiles in the *HST*/F160W and ALMA data. The central 1 kpc regions are located above the star formation main-sequence and have higher sSFRs than those in the

outer disk, indicating the centrally-rising sSFR profiles. This result supports an outside-in transformation scenario in which a dense core is formed at the center of a more extended disk, likely via dissipative in-disk inflows.

6. The compact starburst could put most of massive SFGs on the mass-size relation for QGs at $z \sim 2$ within 300 Myr if the current star formation activity and its spatial distribution are maintained. The averaged evolution in the mass-size plane is approximated by $\Delta \log R_e = -0.3 \Delta \log M_*$. We also found that 38% of massive SFGs can form a dense core with $\log(M_{1\text{kpc}}/M_\odot) = 10.5$ within 300 Myr. Some of the remaining ones may need to make their distribution of star formation more compact by further dissipative processes.

The compact dust emission in our ALMA sample appears to be inconsistent with previous results that the $\text{H}\alpha$ emission is more extended than the stellar continuum emission in less massive, less dusty SFGs at $z \sim 2$ (Suzuki et al. 2019; Wilman et al. 2020). Note that our targets are all massive SFGs with $\log(M_*/M_\odot) > 11$, where most of star formation is obscured by dust. In the stellar mass range of $\log(M_*/M_\odot) < 11$, the distribution of dust-obscured star formation is poorly investigated. Deep intermediate ($0''.5$)-resolution ALMA observations, rather than high-resolution ones, are the best for confirming if less massive SFGs form stars in a more extended disk than the spatial extent of previously formed stars and grow from inside out.

One caveat of our study is that we may overestimate the half-mass radius of massive SFGs due to strong dust extinction in the galaxy centers because the current spatially-resolved SED modeling is based on data that does not extend redwards of rest-frame 5000 \AA , provided by *HST*/F160W-band observations. If this is true, the half-mass radius could be as compact as the 870 μm emission and the Sérsic index could already reach $n = 4$. In that case, massive SFGs do not have to transform their morphology in term of both size and radial profile (core mass). At this moment, there is no evidence supporting the possibility that the half-mass radius is overestimated by a factor of two. It is definitely important to verify if the stellar mass distribution is surely more extended than the dust in massive SFGs. They are sufficiently bright at 3–4 μm , where the emission is less affected by dust extinction, with an AB magnitude of 20–21. High-resolution 3–4 μm observations with Near Infrared Camera on the *James Webb Space Telescope* (*JWST*) will allow us to directly probe the stellar mass distribution. The ALMA-*JWST* synergetic observations will provide a definitive answer in the the structural evolution of massive galaxies at the peak of cosmic star formation history.

We are very grateful to the referee for constructive suggestions to improve the paper. We thank Pieter van Dokkum for comments on the first draft of the paper. This paper makes use of the following ALMA data: ADS/JAO.ALMA#2017.1.01027.S (primary), 2012.1.00245.S, 2012.1.00983.S, 2013.1.00205.S, 2013.1.00566.S, 2013.1.00884.S, 2015.1.00242.S, 2016.1.01079.S. ALMA is a partnership of ESO

(representing its member states), NSF (USA) and NINS (Japan), together with NRC (Canada) and NSC and ASIAA (Taiwan) and KASI (Republic of Korea), in cooperation with the Republic of Chile. The Joint ALMA Observatory is operated by ESO, AUI/NRAO and NAOJ. K.T. acknowledges support by JSPS KAKENHI Grant Number JP20K14526. E.W. acknowledges support by the Australian Research Council Centre of Excellence for All Sky Astrophysics in 3 Dimensions (ASTRO 3D), through project number CE170100013. Data analysis was in part carried out on the common-use data analysis computer system at the Astronomy Data Center (ADC) of the National Astronomical Observatory of Japan. This research made use of `UVMULTIFIT` and `stacker`, software tools developed by the Nordic ALMA Regional Center. The Nordic ARC node is funded through Swedish Research Council grant No 2017-00648.

APPENDIX A

ALMA IMAGES AND CATALOGS

We present the catalogs for our ALMA sample (Table 1 and Table 2). Figure 12 shows the spatial distributions of the 870 μm continuum emission on the *HST*/F160W-band images for 62 galaxies detected at $S/N > 10$ in the ALMA intermediate-resolution images. As 27 of them are not detected at $S/N > 10$ in the high-resolution images, we overlay the contours of the 870 μm emission in the intermediate-resolution images, that are sensitive to an extended component. The 870 μm emission is smoothly distributed and does not have multiple components like star-forming clumps in disks (e.g., Hodge et al. 2016; Rujopakarn et al. 2019). The centrally-concentrated component is the primary star-forming region in massive SFGs as most of star formation is obscured by dust. Figure 13 shows the comparison of the effective radius between ALMA/870 μm and *HST*/F160W-band, demonstrating the result that the dust emission is more compact than the optical emission.

APPENDIX B

MEASUREMENTS OF STRUCTURAL PARAMETERS THROUGH VISIBILITY FITTING

Using the `CASA Toolkit`, we simulate ALMA observations to evaluate the uncertainties of the size measurements through visibility fitting. First, we generate elliptical Gaussian models with six free parameters: centroid position, flux density, full width at half maximum (FWHM), minor-to-major axis ratio q_{FIR} , and position angle PA_{FIR} . The position angle is defined as counter-clockwise from North in the images. Next, we add them as a mock source to the observed visibility data for 2 non-detected objects (U4-17264 and U4-21087). The flux density varies from 0.3 mJy to 2.6 mJy with a step of 0.1 mJy, the FWHM varies from $0''.1$ to $1''.5$ with a step of $0''.1$ and the axis ratio varies from 0.2 to 1.0 with a step of 0.1, resulting in a total of 6280 mock sources. The centroid position is random within the range from $-3''$ to $+3''$ from the phase center and the position angle is random. Then, we create intermediate-resolution images in the same way as in Section 2.4 to derive the S/N of the mock sources. When the mock source is detected at $S/N > 5$, we fit elliptical Gaussian models to the visibility data by using the `UVMULTIFIT`. The structural param-

eters derived from the best-fit model are compared to the input parameters in three bins: $S/N=5-6$, $S/N=10-11$ and $S/N=15-16$ (Figure 14).

The simulations demonstrate the flux measurements work well even at $S/N=5$ (Figure 14). The uncertainties in the size measurements are typically $\Delta\text{FWHM}=\pm 0''.2$ at $S/N=5$, $\Delta\text{FWHM}=\pm 0''.1$ at $S/N=10$, and $\Delta\text{FWHM}=\pm 0''.05$ at $S/N=15$. Only when the measured size is as small as $\text{FWHM}=0''.1$ at $S/N=5$, it is underestimated by a factor of 4. Measuring the axis ratio requires at least $S/N=10$ where the uncertainties are $\Delta q=\pm 0.15$. It seems to be reasonable to adopt circular Gaussian models for measuring the size of the dust emission in $5 < S/N < 10$ sources. The important thing here is that there are no systematic errors in the measurement of size over a wide range from $\text{FWHM}=0''.1$ to $1''.5$ in $S/N > 10$ conditions. We therefore use only $S/N > 10$ sources for discussion of the size measurements at 870 μm .

When more than one source is detected in the observed field, we use two- or three-component models for the fitting. We simply assume circular Gaussian models for the second and the third component to reduce the free parameters. Even when taking into account the contribution of additional sources, the measurement results only change one percent, except for the two cases where a bright companion is located within $1''.5$ of the primary targets (U4-7472 and U4-36568).

For visualization of the visibility fitting, we compute the uv distances along the minor axis $u'v'$ as

$$\begin{aligned} u' &= u \cos \theta - v \sin \theta, \\ v' &= (u \sin \theta + v \cos \theta) \times q_{\text{FIR}}, \\ u'v' &= \sqrt{u'^2 + v'^2}, \end{aligned} \quad (6)$$

where $\theta=90+\text{PA}_{\text{FIR}}$. The minor axis in the visibility plane corresponds to the major axis in the image. We extract the spatial frequency (u,v) and the real/imaginary part of individual visibility by using `CASA/plotms` to derive the $u'v'$ distance and the amplitudes. The amplitudes are computed as the norm of the visibility vectors, averaged in each $u'v'$ bin. In the right panels of Figure 5, we show the amplitudes of the visibilities as a function of the $u'v'$ distance, for both cases of compact and extended sources. We note that `UVMULTIFIT` fits individual visibility data, not the averaged one. In Figure 15, we show the amplitude plots along with the best-fit models for the ALMA sample of 62 galaxies detected at $S/N > 10$. They are used only for visually checking the fitting results. The amplitudes of extended sources rapidly decline as $u'v'$ distance while those of compact sources slowly change. As the Fourier transform of the Gaussian function in the image plane is a Gaussian function in the visibility plane, its spatial extent is derived as $\text{FWHM}_{\text{image}} [\text{arcsec}] = 182 / \text{FWHM}_{\text{visibility}} [\text{k}\lambda]$. Our ALMA observations demonstrate that visibility data at a very high spatial frequency ($uv > 1000 \text{ k}\lambda$) is inefficient for measuring the size of the dust emission for massive SFGs at $z \sim 2$ since most of them have $\text{FWHM}_{\text{image}} > 0''.15$ corresponding to $uv < 600 \text{ k}\lambda$.

APPENDIX C

CALCULATIONS OF THE CENTRAL STELLAR MASS AND THE EFFECTIVE RADIUS

The calculation of the central stellar mass is not straightforward when based on the three-dimensional profile ρ . Following (Bezanson et al. 2009), we deproject the two-dimensional Sérsic profile using an Abel transform:

$$\rho(x) \propto x^{1/n-1} \int_1^\infty \frac{\exp(-b_n x^{1/n} t)}{\sqrt{t^{2n} - 1}} dt \quad (7)$$

where $x = r/R_{\text{eff,circ}}$ and $R_{\text{eff,circ}}$ is given by $R_{\text{eff}}\sqrt{q}$. The mass of newly formed stars is given by equation 5. Then, we numerically compute the central mass as

$$M_{1\text{kpc}} = \int_0^{1\text{kpc}} \rho_{HST}(x_{HST}) 4\pi r^2 dr + \int_0^{1\text{kpc}} \rho_{ALMA}(x_{ALMA}) 4\pi r^2 dr. \quad (8)$$

where ρ_{HST} and ρ_{ALMA} are the 3D mass profile of already existing and newly formed stars, respectively. The time evolution of the circularized effective radius can be inferred from the 2D mass profiles (Σ_{HST} and Σ_{ALMA}), which are derived from the best-fitting Sérsic profile in the *HST* and ALMA data, respectively. We numerically compute the circularized effective radius that satisfies

$$\frac{M_\star + M_{\star,\text{new}}}{2} = \int_0^{R_{\text{eff,circ}}} \Sigma_{HST}(r) 2\pi r dr + \int_0^{R_{\text{eff,circ}}} \Sigma_{ALMA}(r) 2\pi r dr. \quad (9)$$

REFERENCES

- Barro, G., Faber, S. M., Pérez-González, P. G., et al. 2013, *ApJ*, 765, 104
— 2014, *ApJ*, 791, 52
Barro, G., Kriek, M., Pérez-González, P. G., et al. 2016, *ApJL*, 827, L32
Bell, E. F., van der Wel, A., Papovich, C., et al. 2012, *ApJ*, 753, 167
Belli, S., Genzel, R., Förster Schreiber, N. M., et al. 2017, *ApJL*, 841, L6
Bezanson, R., van Dokkum, P. G., Tal, T., et al. 2009, *ApJ*, 697, 1290
Bournaud, F., Perret, V., Renaud, F., et al. 2014, *ApJ*, 780, 57
Bruce, V. A., Dunlop, J. S., Cirasuolo, M., et al. 2012, *MNRAS*, 427, 1666
Bruzual, G., & Charlot, S. 2003, *MNRAS*, 344, 1000
Calistro Rivera, G., Hodge, J. A., Smail, I., et al. 2018, *ApJ*, 863, 56
Calzetti, D., Armus, L., Bohlin, R. C., et al. 2000, *ApJ*, 533, 682
Chabrier, G. 2003, *PASP*, 115, 763
Chen, C.-C., Hodge, J. A., Smail, I., et al. 2017, *ApJ*, 846, 108
Chen, C.-C., Harrison, C. M., Smail, I., et al. 2020, *A&A*, 635, A119
Cochrane, R. K., Hayward, C. C., Anglés-Alcázar, D., et al. 2019, *MNRAS*, 488, 1779
Conselice, C. J. 2014, *ARA&A*, 52, 291
Daddi, E., Renzini, A., Pirzkal, N., et al. 2005, *ApJ*, 626, 680
Dekel, A., & Burkert, A. 2014, *MNRAS*, 438, 1870
Elbaz, D., Leiton, R., Nagar, N., et al. 2018, *A&A*, 616, A110
Forbes, J. C., Krumholz, M. R., Burkert, A., & Dekel, A. 2014, *MNRAS*, 438, 1552
Förster Schreiber, N. M., Renzini, A., Mancini, C., et al. 2018, *ApJS*, 238, 21
Franco, M., Elbaz, D., Béthermin, M., et al. 2018, *A&A*, 620, A152
Franx, M., van Dokkum, P. G., Förster Schreiber, N. M., et al. 2008, *ApJ*, 688, 770
Fujimoto, S., Ouchi, M., Kohno, K., et al. 2018, *ApJ*, 861, 7
Geach, J. E., Dunlop, J. S., Halpern, M., et al. 2017, *MNRAS*, 465, 1789
Genzel, R., Tacconi, L. J., Eisenhauer, F., et al. 2006, *Nature*, 442, 786
Genzel, R., Tacconi, L. J., Lutz, D., et al. 2015, *ApJ*, 800, 20
Goddard, D., Thomas, D., Maraston, C., et al. 2017, *MNRAS*, 466, 4731
Grogin, N. A., Kocevski, D. D., Faber, S. M., et al. 2011, *ApJS*, 197, 35
Gullberg, B., Smail, I., Swinbank, A. M., et al. 2019, *MNRAS*, 490, 4956
Hayward, C. C., Lanz, L., Ashby, M. L. N., et al. 2014, *MNRAS*, 445, 1598
Hodge, J. A., Swinbank, A. M., Simpson, J. M., et al. 2016, *ApJ*, 833, 103
Ikarashi, S., Ivison, R. J., Caputi, K. I., et al. 2015, *ApJ*, 810, 133
Immeli, A., Samland, M., Gerhard, O., & Westera, P. 2004, *A&A*, 413, 547
Kennicutt, Robert C., J. 1998, *ARA&A*, 36, 189
Koekemoer, A. M., Faber, S. M., Ferguson, H. C., et al. 2011, *ApJS*, 197, 36
Kriek, M., van Dokkum, P. G., Labbé, I., et al. 2009, *ApJ*, 700, 221
Kurk, J., Cimatti, A., Daddi, E., et al. 2013, *A&A*, 549, A63
Lang, P., Wuyts, S., Somerville, R. S., et al. 2014, *ApJ*, 788, 11
Lang, P., Schinnerer, E., Smail, I., et al. 2019, *ApJ*, 879, 54
Law, D. R., Steidel, C. C., Shapley, A. E., et al. 2012, *ApJ*, 745, 85
Leja, J., Johnson, B. D., Conroy, C., et al. 2019, *ApJ*, 877, 140
Lilly, S. J., & Carollo, C. M. 2016, *ApJ*, 833, 1
Lindroos, L., Knudsen, K. K., Vlemmings, W., Conway, J., & Martí-Vidal, I. 2015, *MNRAS*, 446, 3502
Lutz, D., Poglitsch, A., Altieri, B., et al. 2011, *A&A*, 532, A90
Madau, P., & Dickinson, M. 2014, *ARA&A*, 52, 415
Magnelli, B., Popesso, P., Berta, S., et al. 2013, *A&A*, 553, A132
Martí-Vidal, I., Vlemmings, W. H. T., Muller, S., & Casey, S. 2014, *A&A*, 563, A136
McMullin, J. P., Waters, B., Schiebel, D., Young, W., & Golap, K. 2007, *Astronomical Society of the Pacific Conference Series*, Vol. 376, *CASA Architecture and Applications*, ed. R. A. Shaw, F. Hill, & D. J. Bell, 127
Momcheva, I. G., Brammer, G. B., van Dokkum, P. G., et al. 2016, *ApJS*, 225, 27
Mosleh, M., Tacchella, S., Renzini, A., et al. 2017, *ApJ*, 837, 2
Mowla, L. A., van Dokkum, P., Brammer, G. B., et al. 2019, *ApJ*, 880, 57
Naab, T., Johansson, P. H., & Ostriker, J. P. 2009, *ApJL*, 699, L178
Nelson, E., van Dokkum, P., Franx, M., et al. 2014, *Nature*, 513, 394
Nelson, E. J., van Dokkum, P. G., Momcheva, I. G., et al. 2016a, *ApJL*, 817, L9
Nelson, E. J., van Dokkum, P. G., Förster Schreiber, N. M., et al. 2016b, *ApJ*, 828, 27
Nelson, E. J., Tadaki, K.-i., Tacconi, L. J., et al. 2019, *ApJ*, 870, 130
Newman, A. B., Belli, S., Ellis, R. S., & Patel, S. G. 2018a, *ApJ*, 862, 125
— 2018b, *ApJ*, 862, 126
Newman, A. B., Ellis, R. S., Bundy, K., & Treu, T. 2012, *ApJ*, 746, 162
Noguchi, M. 1999, *ApJ*, 514, 77
Pavesi, R., Sharon, C. E., Riechers, D. A., et al. 2018, *ApJ*, 864, 49
Peng, Y.-j., Lilly, S. J., Kovač, K., et al. 2010, *ApJ*, 721, 193
Popesso, P., Dickinson, M., Nonino, M., et al. 2009, *A&A*, 494, 443
Price, S. H., Kriek, M., Feldmann, R., et al. 2017, *ApJL*, 844, L6
Retzlaff, J., Rosati, P., Dickinson, M., et al. 2010, *A&A*, 511, A50

- Rujopakarn, W., Dunlop, J. S., Rieke, G. H., et al. 2016, *ApJ*, 833, 12
- Rujopakarn, W., Daddi, E., Rieke, G. H., et al. 2019, *ApJ*, 882, 107
- Scoville, N., Sheth, K., Aussel, H., et al. 2016, *ApJ*, 820, 83
- Sérsic, J. L. 1963, *Boletín de la Asociación Argentina de Astronomía La Plata Argentina*, 6, 41
- Simpson, J. M., Smail, I., Swinbank, A. M., et al. 2015a, *ApJ*, 807, 128
- . 2015b, *ApJ*, 799, 81
- Skelton, R. E., Whitaker, K. E., Momcheva, I. G., et al. 2014, *ApJS*, 214, 24
- Stach, S. M., Dudzevičiūtė, U., Smail, I., et al. 2019, *MNRAS*, 487, 4648
- Suess, K. A., Bezanson, R., Spilker, J. S., et al. 2017, *ApJL*, 846, L14
- Suess, K. A., Kriek, M., Price, S. H., & Barro, G. 2019, *ApJ*, 877, 103
- Suzuki, T. L., Minowa, Y., Koyama, Y., et al. 2019, *PASJ*, 71, 69
- Szokoly, G. P., Bergeron, J., Hasinger, G., et al. 2004, *ApJS*, 155, 271
- Tacchella, S., Dekel, A., Carollo, C. M., et al. 2016, *MNRAS*, 457, 2790
- Tacchella, S., Carollo, C. M., Renzini, A., et al. 2015, *Science*, 348, 314
- Tacchella, S., Carollo, C. M., Förster Schreiber, N. M., et al. 2018, *ApJ*, 859, 56
- Tacconi, L. J., Genzel, R., Saintonge, A., et al. 2018, *ApJ*, 853, 179
- Tadaki, K.-i., Kodama, T., Tanaka, I., et al. 2013, *ApJ*, 778, 114
- Tadaki, K.-i., Kohno, K., Kodama, T., et al. 2015, *ApJL*, 811, L3
- Tadaki, K.-i., Genzel, R., Kodama, T., et al. 2017a, *ApJ*, 834, 135
- Tadaki, K.-i., Kodama, T., Nelson, E. J., et al. 2017b, *ApJL*, 841, L25
- Tadaki, K.-i., Iono, D., Hatsukade, B., et al. 2019, *ApJ*, 876, 1
- Tadaki, K.-i., Iono, D., Yun, M. S., et al. 2020, *ApJ*, 889, 141
- Toft, S., Zabl, J., Richard, J., et al. 2017, *Nature*, 546, 510
- Trujillo, I., Feulner, G., Goranova, Y., et al. 2006, *MNRAS*, 373, L36
- Umehata, H., Smail, I., Swinbank, A. M., et al. 2020, *arXiv e-prints*, arXiv:2007.09887
- Utomo, D., Kriek, M., Labbé, I., Conroy, C., & Fumagalli, M. 2014, *ApJL*, 783, L30
- van der Wel, A., Bell, E. F., Häussler, B., et al. 2012, *ApJS*, 203, 24
- van der Wel, A., Franx, M., van Dokkum, P. G., et al. 2014, *ApJ*, 788, 28
- van Dokkum, P. G., Franx, M., Kriek, M., et al. 2008, *ApJL*, 677, L5
- van Dokkum, P. G., Bezanson, R., van der Wel, A., et al. 2014, *ApJ*, 791, 45
- van Dokkum, P. G., Nelson, E. J., Franx, M., et al. 2015, *ApJ*, 813, 23
- Wang, T., Schreiber, C., Elbaz, D., et al. 2019, *Nature*, 572, 211
- Whitaker, K. E., Pope, A., Cybulski, R., et al. 2017, *ApJ*, 850, 208
- Whitaker, K. E., Labbé, I., van Dokkum, P. G., et al. 2011, *ApJ*, 735, 86
- Whitaker, K. E., Franx, M., Leja, J., et al. 2014, *ApJ*, 795, 104
- Whitaker, K. E., Franx, M., Bezanson, R., et al. 2015, *ApJL*, 811, L12
- Williams, C. C., Giavalisco, M., Cassata, P., et al. 2014, *ApJ*, 780, 1
- Williams, C. C., Labbe, I., Spilker, J., et al. 2019, *ApJ*, 884, 154
- Wilman, D. J., Fossati, M., Mendel, J. T., et al. 2020, *ApJ*, 892, 1
- Wisnioski, E., Förster Schreiber, N. M., Wuyts, S., et al. 2015, *ApJ*, 799, 209
- Wisnioski, E., Mendel, J. T., Förster Schreiber, N. M., et al. 2018, *ApJ*, 855, 97
- Wisnioski, E., Förster Schreiber, N. M., Fossati, M., et al. 2019, *ApJ*, 886, 124
- Wuyts, S., Labbé, I., Förster Schreiber, N. M., et al. 2008, *ApJ*, 682, 985
- Wuyts, S., Labbé, I., Franx, M., et al. 2007, *ApJ*, 655, 51
- Wuyts, S., Förster Schreiber, N. M., van der Wel, A., et al. 2011a, *ApJ*, 742, 96
- Wuyts, S., Förster Schreiber, N. M., Lutz, D., et al. 2011b, *ApJ*, 738, 106
- Wuyts, S., Förster Schreiber, N. M., Genzel, R., et al. 2012, *ApJ*, 753, 114
- Yamaguchi, Y., Kohno, K., Hatsukade, B., et al. 2019, *ApJ*, 878, 73
- Zlotov, A., Dekel, A., Mandelker, N., et al. 2015, *MNRAS*, 450, 2327

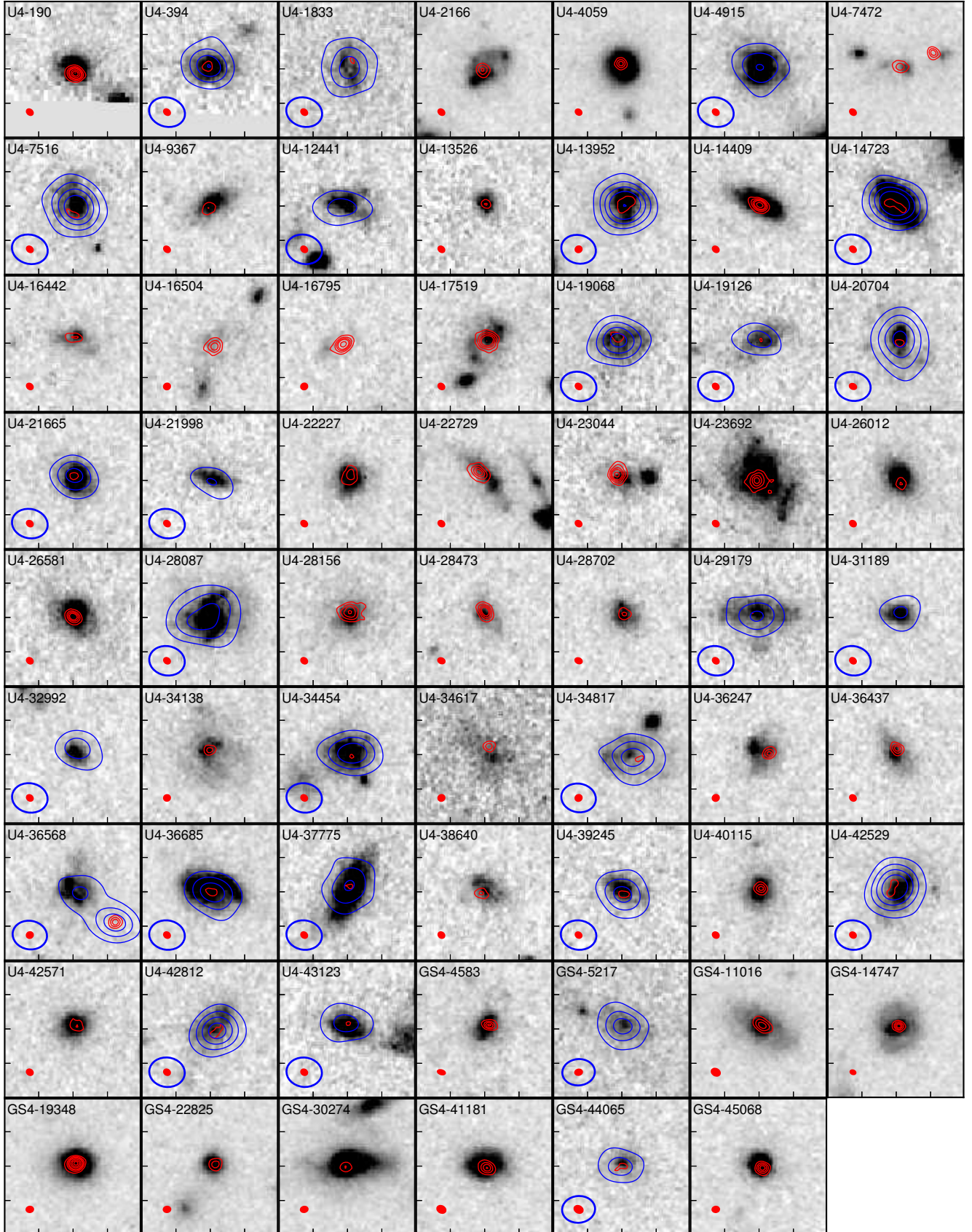


Figure 12. The *HST*/F160W-band images ($4'' \times 4''$) for our ALMA sample of 62 massive galaxies. Red contours display the $870 \mu\text{m}$ flux densities in the ALMA high-resolution images. For galaxies detected at $S/N < 10$ in the high-resolution images, we overlay blue contours of the $870 \mu\text{m}$ flux densities in the intermediate-resolution images. Both contours are plotted every 5σ to 20σ and every 10σ from 20σ . Red and blue ellipses in the bottom left corner show the synthesized beams of the high-resolution and the intermediate-resolution images, respectively. The geometric offset between ALMA and *HST* astrometry was corrected in these images (section 4.1).

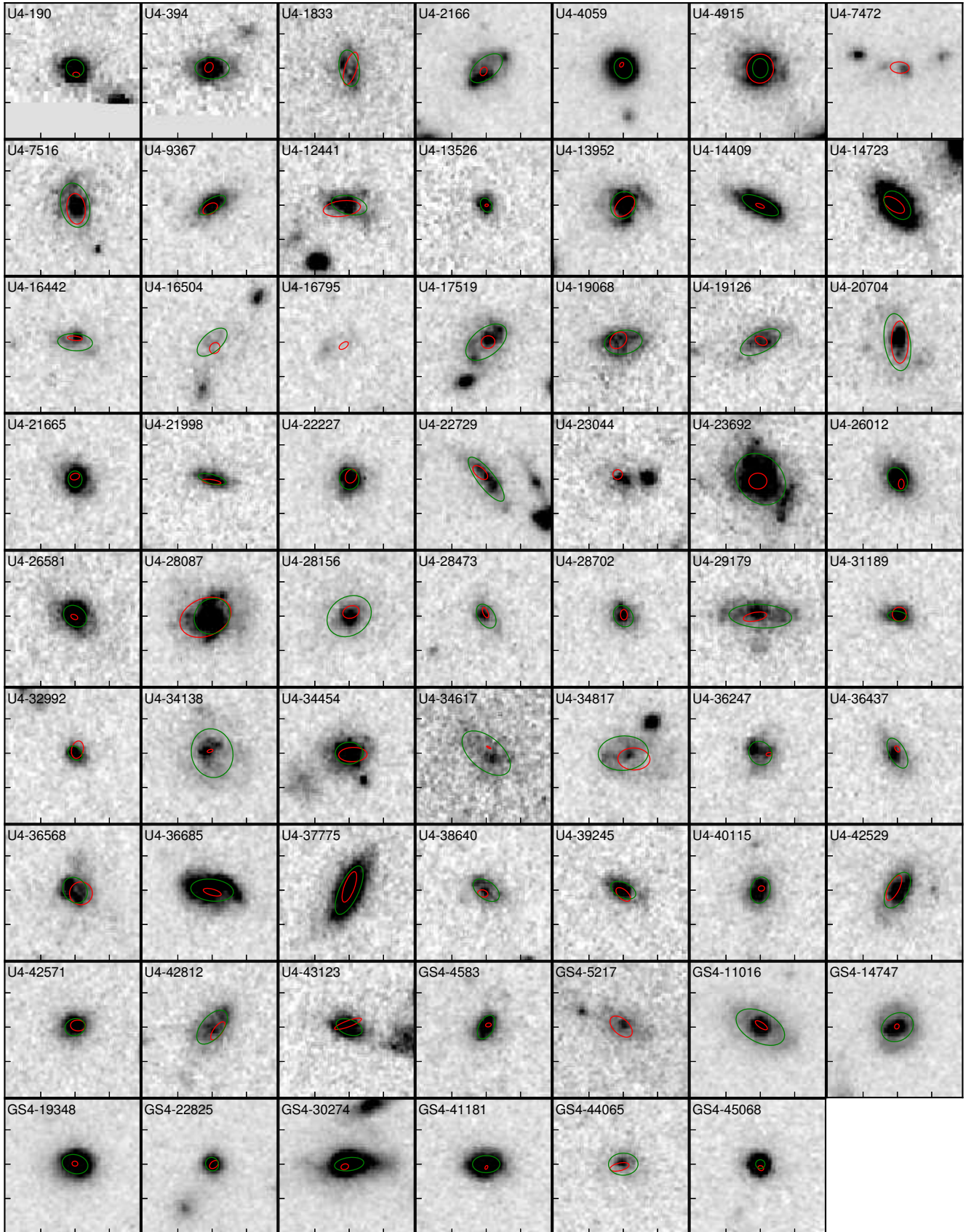


Figure 13. The same as Figure 12. Red and green ellipses are based on the structural parameters (centroid, effective radius, minor-to-major axis ratio and position angle) from the best-fitting Sérsic profile in the ALMA/870 μm and the *HST*/F160W-band data, respectively.

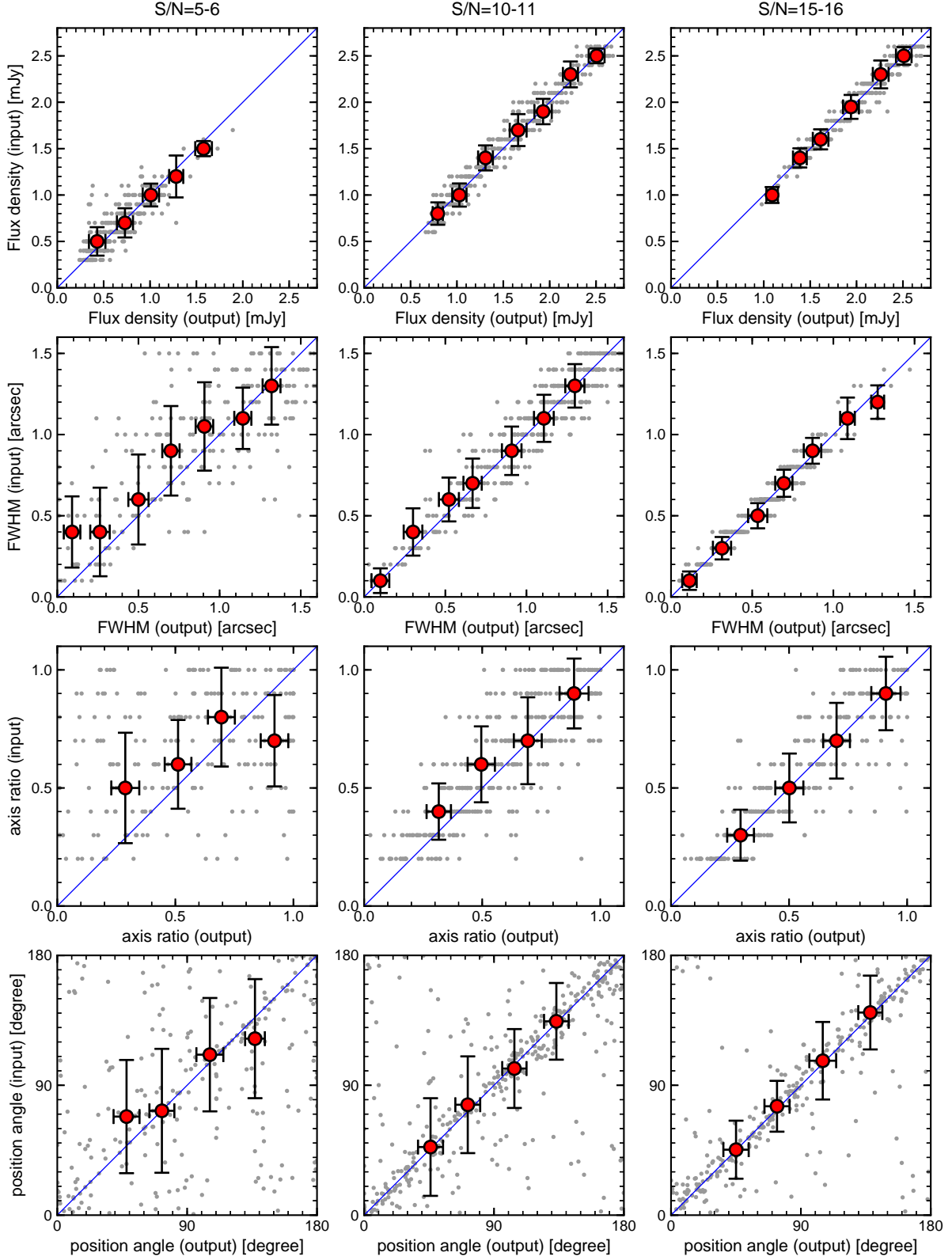


Figure 14. Comparisons of structural parameters (flux density, FWHM, minor-to-major axis ratio and position angle) between measurements by fitting to the simulated visibility data (output) and input models in 6280 mock sources. Left, middle and right panels show the simulation results for sources detected at $S/N = 5 - 6$, $S/N = 10 - 11$ and $S/N = 15 - 16$ in the intermediate-resolution images, respectively. Red circles and the error bars indicate the median and the standard deviation in the bins of output values.

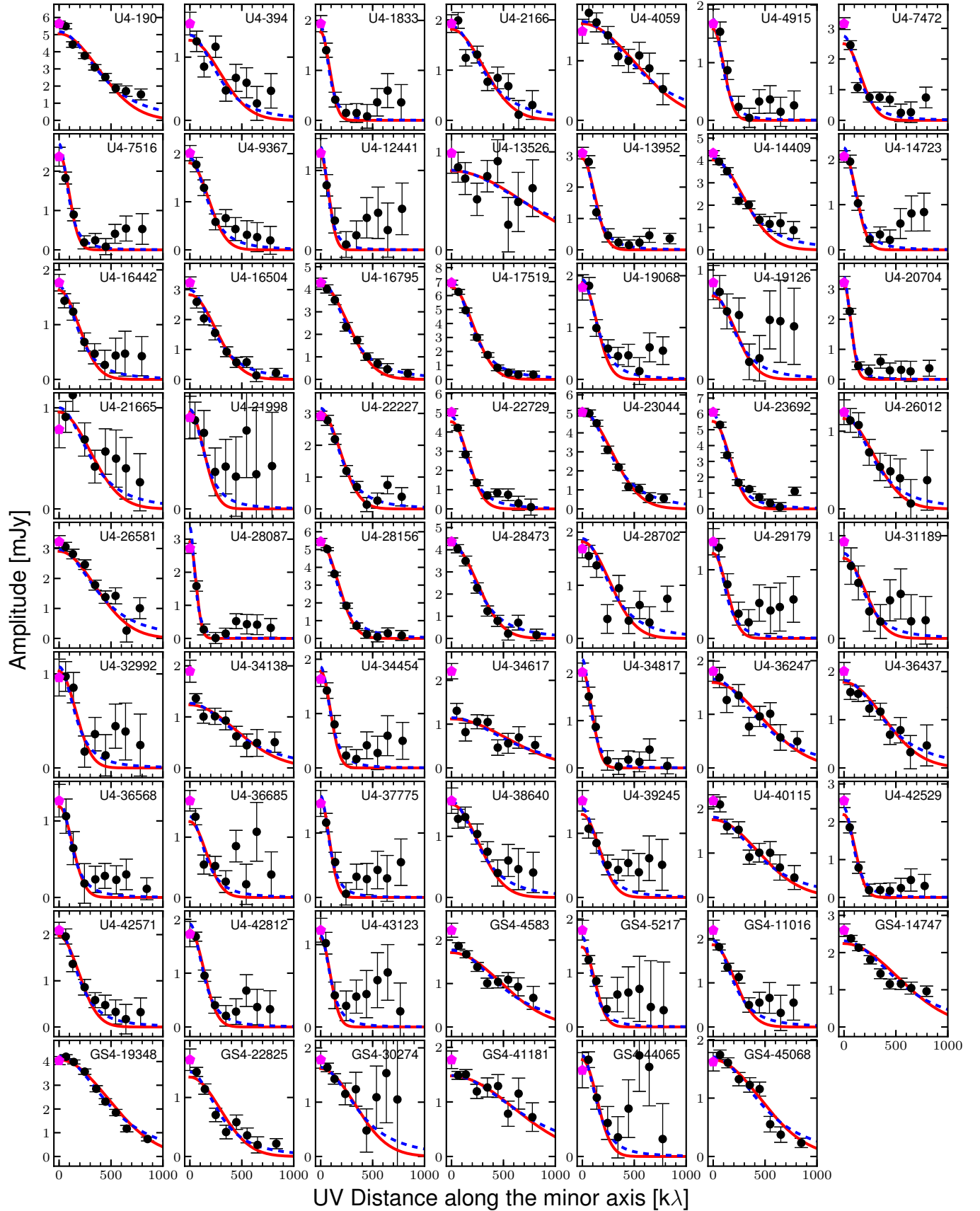


Figure 15. Visibility amplitudes versus uv distances for our sample of 62 massive SFGs detected at $S/N > 10$ in the intermediate-resolution images. The symbols are the same as Figure 5.

Table 1
The source list of 85 massive star-forming galaxies.

ID ^a	R.A. (degree)	Decl. (degree)	z ^b	log M_* (M_\odot)	log SFR ($M_\odot \text{yr}^{-1}$)	$R_{e,\text{opt}}$ ^c (kpc)	q_{opt} ^c	S/N ^d	S_{image} ^e (mJy)	log M_{gas} (M_\odot)
U4-190	34.2654	-5.2776	2.06	11.23	3.14	2.2	0.92	80.2	5.64 ± 0.14	11.48
U4-394	34.3965	-5.2768	2.28	11.11	2.68	4.1	0.62	20.0	1.53 ± 0.18	10.92
U4-1620	34.3582	-5.2726	2.3185	11.27	0.27	1.3	0.90	2.4	<0.83	<10.65
U4-1833	34.3766	-5.2713	2.51	11.28	2.72	4.3	0.55	17.7	1.94 ± 0.16	11.02
U4-2166	34.4264	-5.2710	2.11	11.07	3.03	4.6	0.54	29.1	1.93 ± 0.18	11.01
U4-2394	34.5096	-5.2695	2.31	11.11	2.60	2.0	0.51	6.9	0.61 ± 0.19	10.52
U4-4059	34.4374	-5.2642	2.323	11.09	2.57	2.5	0.85	24.2	1.49 ± 0.20	10.91
U4-4499	34.5142	-5.2615	2.1813	11.16	-0.54	0.7	0.54	2.3	<0.74	<10.60
U4-4701	34.2733	-5.2621	2.1065	11.49	-0.22	1.8	0.62	1.9	<0.98	<10.72
U4-4706	34.2882	-5.2626	2.5217	11.24	2.17	5.2	0.44 ± 0.17	10.38
U4-4915	34.3478	-5.2612	1.907	11.13	2.26	2.4	0.80	15.1	1.68 ± 0.25	10.95
U4-7472	34.4654	-5.2520	2.093	11.52	2.41	34.4	3.16 ± 0.19	11.23
U4-7516	34.4899	-5.2524	2.080	11.30	2.26	5.4	0.64	25.6	2.37 ± 0.24	11.10
U4-9367	34.3316	-5.2453	2.009	11.25	2.25	3.7	0.42	24.9	2.01 ± 0.16	11.03
U4-12441	34.5847	-5.2348	1.99	11.12	2.31	4.4	0.51	12.5	1.22 ± 0.18	10.81
U4-13526	34.5248	-5.2308	2.49	11.21	2.32	1.7	0.72	13.6	0.99 ± 0.21	10.73
U4-13952	34.3226	-5.2300	2.1830	11.32	2.24	3.4	0.89	30.0	3.08 ± 0.18	11.22
U4-14409	34.3070	-5.2281	2.17	11.21	2.38	4.8	0.36	64.8	4.33 ± 0.11	11.37
U4-14723	34.5298	-5.2277	1.92	11.41	2.57	4.0	0.63	28.5	2.07 ± 0.13	11.04
U4-14996	34.2789	-5.2266	2.082	11.32	1.78	2.3	0.80	6.6	0.68 ± 0.13	10.56
U4-16022	34.5520	-5.2223	2.40	11.34	2.00	6.5	0.19	6.0	0.46 ± 0.14	10.39
U4-16442	34.3367	-5.2211	2.193	11.20	2.22	4.2	0.49	25.2	1.77 ± 0.15	10.98
U4-16504	34.4213	-5.2208	2.530	11.25	2.38	4.3	0.51	35.0	3.23 ± 0.19	11.25
U4-16795	34.4188	-5.2196	2.530	11.18	2.62	55.0	4.29 ± 0.20	11.37
U4-17264	34.4058	-5.2189	2.2986	11.14	-0.56	0.9	0.95	2.9	<0.87	<10.67
U4-17519	34.3334	-5.2183	2.385	11.60	2.89	5.6	0.57	92.0	6.92 ± 0.17	11.57
U4-19068	34.4233	-5.2129	2.18	11.15	2.35	4.6	0.63	22.2	1.77 ± 0.24	10.98
U4-19126	34.5870	-5.2126	2.03	11.23	2.21	5.3	0.47	12.7	0.88 ± 0.16	10.67
U4-20704	34.2708	-5.2079	2.1915	11.46	2.36	6.9	0.45	21.6	3.22 ± 0.21	11.24
U4-21087	34.2832	-5.2060	2.3168	11.11	-0.59	1.0	0.94	1.8	<0.76	<10.61
U4-21665	34.4902	-5.2040	1.964	11.03	1.83	2.0	0.85	16.9	0.79 ± 0.18	10.62
U4-21998	34.5178	-5.2023	2.11	11.05	1.81	3.5	0.32	10.2	0.64 ± 0.15	10.53
U4-22227	34.4242	-5.2019	2.2896	11.27	2.36	2.5	0.94	42.7	2.92 ± 0.15	11.20
U4-22729	34.4693	-5.2010	2.579	11.34	2.75	6.4	0.31	63.9	5.03 ± 0.18	11.44
U4-23044	34.3857	-5.1990	2.421	11.61	3.08	76.4	5.09 ± 0.20	11.44
U4-23692	34.3632	-5.1994	2.031	11.64	2.91	6.9	0.79	72.1	6.11 ± 0.18	11.51
U4-26012	34.2653	-5.1895	2.3208	11.06	2.41	3.0	0.72	17.8	1.25 ± 0.16	10.83
U4-26581	34.5491	-5.1877	2.22	11.24	2.50	3.0	0.79	45.1	3.23 ± 0.20	11.24
U4-28087	34.3588	-5.1828	2.113	11.34	2.30	4.6	0.89	17.1	2.72 ± 0.15	11.16
U4-28156	34.4685	-5.1824	1.995	11.36	2.51	5.7	0.81	71.1	5.44 ± 0.19	11.46
U4-28473	34.4224	-5.1810	2.5247	11.35	2.59	3.1	0.62	54.7	4.36 ± 0.17	11.38
U4-28702	34.4775	-5.1800	2.190	11.03	2.10	2.7	0.81	22.9	1.69 ± 0.17	10.96
U4-29179	34.5888	-5.1789	2.006	11.39	2.10	7.7	0.37	15.9	1.41 ± 0.19	10.87
U4-30882	34.2294	-5.1730	2.1057	11.01	0.01	0.9	0.66	1.1	<0.91	<10.69
U4-31189	34.4158	-5.1719	2.294	11.16	2.40	2.4	0.51	10.8	0.94 ± 0.19	10.71
U4-32147	34.3996	-5.1693	2.5294	11.15	1.90	4.5	0.52	8.5	0.84 ± 0.16	10.66
U4-32351	34.3061	-5.1682	2.1800	11.04	2.17	3.4	0.70	9.3	0.84 ± 0.18	10.65
U4-32992	34.4727	-5.1657	2.182	11.01	2.21	2.0	0.74	13.1	0.96 ± 0.20	10.71
U4-34138	34.4086	-5.1631	2.5186	11.05	2.23	5.8	0.84	18.3	1.90 ± 0.22	11.01
U4-34454	34.2867	-5.1615	2.027	11.18	2.36	3.4	0.79	19.4	1.63 ± 0.13	10.94
U4-34617	34.4785	-5.1606	2.530	11.04	2.42	6.8	0.55	17.6	2.21 ± 0.18	11.08
U4-34817	34.2718	-5.1601	2.190	11.21	2.37	6.0	0.69	18.0	2.02 ± 0.19	11.04
U4-36247	34.2817	-5.1548	2.1790	11.04	2.41	3.0	0.89	23.3	1.80 ± 0.19	10.99
U4-36437	34.4852	-5.1542	2.083	11.13	2.47	4.0	0.49	27.2	2.01 ± 0.18	11.03
U4-36568	34.2938	-5.1545	2.1770	11.05	2.40	3.3	0.84	10.9	1.26 ± 0.21	10.83
U4-36685	34.2893	-5.1538	1.95	11.38	2.48	5.2	0.51	19.0	1.60 ± 0.17	10.93
U4-37775	34.5325	-5.1503	1.92	11.49	2.43	6.4	0.36	15.5	1.46 ± 0.20	10.89
U4-38040	34.4687	-5.1481	2.49	11.02	2.08	3.6	0.49	7.6	0.43 ± 0.17	10.37
U4-38640	34.5595	-5.1460	2.42	11.25	2.39	3.5	0.59	21.5	1.58 ± 0.21	10.93
U4-39126	34.5498	-5.1444	2.02	11.13	2.08	6.8	0.31	6.3	0.54 ± 0.19	10.46
U4-39245	34.5539	-5.1438	2.12	11.14	2.42	3.2	0.55	17.3	1.51 ± 0.16	10.91
U4-39537	34.4820	-5.1437	2.0234	11.24	2.09	2.2	0.82	3.7	<0.69	<10.56
U4-40115	34.4408	-5.1411	2.02	11.08	2.47	3.2	0.72	28.6	2.18 ± 0.14	11.06
U4-41248	34.3150	-5.1356	1.9210	11.01	0.82	1.3	0.84	2.5	<0.91	<10.68
U4-42529	34.4454	-5.1305	2.39	11.53	2.58	4.7	0.52	26.4	2.56 ± 0.18	11.14
U4-42571	34.4331	-5.1309	2.41	11.38	2.52	2.4	0.82	26.9	2.10 ± 0.17	11.06
U4-42812	34.2675	-5.1296	2.12	11.16	2.41	4.9	0.54	23.0	1.73 ± 0.24	10.97
U4-43123	34.5208	-5.1289	2.03	11.04	2.31	3.3	0.55	12.1	1.17 ± 0.14	10.80
U4-43667	34.2584	-5.1266	2.04	11.15	1.90	5.8	0.68	6.4	0.92 ± 0.15	10.69
GS4-1397	53.1040	-27.9226	2.5552	11.03	0.58	3.5	0.48	3.5	<0.84	<10.66
GS4-1725	53.2049	-27.9179	2.206	11.03	2.31	2.8	0.66	9.0	0.78 ± 0.28	10.62
GS4-2467	53.2112	-27.9072	2.0404	11.08	1.48	1.1	<0.86	<10.66
GS4-4583	53.1635	-27.8905	2.281	11.11	2.64	3.0	0.58	32.3	2.23 ± 0.16	11.08
GS4-5217	53.1131	-27.8866	2.426	11.02	1.92	17.7	1.79 ± 0.18	10.99

Table 1 — *Continued*

ID ^a	R.A. (degree)	Decl. (degree)	z ^b	log M_* (M_\odot)	log SFR ($M_\odot \text{yr}^{-1}$)	$R_{e,\text{opt}}$ ^c (kpc)	q_{opt} ^c	S/N ^d	S_{image} ^e (mJy)	log M_{gas} (M_\odot)
GS4-11016	53.0773	-27.8596	2.0369	11.24	1.98	6.4	0.58	30.0	2.19 ± 0.22	11.07
GS4-14747	53.0717	-27.8436	1.9560	11.09	2.33	4.1	0.81	42.5	2.60 ± 0.17	11.14
GS4-19348	53.1488	-27.8211	2.5820	11.26	2.91	3.0	0.72	68.7	4.04 ± 0.17	11.34
GS4-22825	53.0940	-27.8041	2.367	11.15	2.03	1.7	0.91	22.1	1.64 ± 0.18	10.95
GS4-30274	53.1311	-27.7731	2.2250	11.20	2.53	3.5	0.44	27.0	1.78 ± 0.16	10.98
GS4-40185	53.0136	-27.7201	2.076	11.14	1.49	6.2	0.74	5.5	0.46 ± 0.15	10.39
GS4-41021	53.1874	-27.7192	2.3135	11.02	2.10	0.5	0.55	-0.1	<0.73	<10.60
GS4-41181	53.1070	-27.7182	2.3001	11.28	2.10	3.3	0.63	27.7	1.77 ± 0.16	10.98
GS4-44065	53.0026	-27.7044	2.59	11.09	2.29	3.4	0.75	12.4	0.73 ± 0.15	10.60
GS4-45068	53.1376	-27.7001	2.4480	11.01	2.56	1.1	0.94	28.7	1.62 ± 0.16	10.94
GS4-45475	53.1737	-27.6981	2.03	11.09	1.89	8.0	0.58	6.4	0.85 ± 0.17	10.65

^a Unique identifier in the 3D-HST v4 catalog (Skelton et al. 2014; Momcheva et al. 2016). U4 and GS4 mean objects in the UDS and the GOODS-S field, respectively.

^b Numbers with 3, 4 and 5 digits means photometric, grism or narrow-band, and spectroscopic redshift, respectively (Section 2.1).

^c Effective radius along the semi-major axis and the minor-to-major axis ratio from the best-fitting Sérsic profile in the *HST*/F160W (van der Wel et al. 2012, 2014; Lang et al. 2014).

^d Signal-to-noise ratio in the ALMA intermediate-resolution images.

^e 870 μm flux densities measured in the ALMA low-resolution images.

Table 2
The galaxy properties of 19 serendipitously detected sources

ID	R.A. (degree)	Decl. (degree)	z ^a	$\log M_*$ (M_\odot)	$\log \text{SFR}$ ($M_\odot \text{yr}^{-1}$)	S/N	S_{image} (mJy)	Primary source ID ^b	Separation ^c (arcsec)	$ \Delta z $ ^d
U4-570	34.3951	-5.2759	2.27	10.87	2.30	12.6	1.04 ± 0.24	U4-394	6.1	0.01
U4-4018	34.3493	-5.2634	2.98	11.37	2.94	8.9	1.75 ± 0.61	U4-4915	9.6	1.07
U4-4303	34.2879	-5.2636	2.454	10.80	1.77	27.2	2.12 ± 0.20	U4-4706	3.8	0.07
U4-4534	34.4388	-5.2636	0.780	10.59	1.66	5.8	0.86 ± 0.27	U4-4059	5.5	1.54
U4-7419	34.4650	-5.2519	2.97	11.24	0.80	29.6	2.36 ± 0.19	U4-7472	1.3	0.88
U4-9997	34.3293	-5.2424	2.77	10.14	2.11	7.3	4.15 ± 0.93	U4-9367	13.3	0.76
U4-14449	34.2775	-5.2281	1.87	10.80	2.24	12.4	1.58 ± 0.21	U4-14996	7.3	0.21
U4-17813	34.5878	-5.2161	4.67	11.69	2.04	8.4	1.85 ± 0.87	U4-19126	13.1	2.64
U4-35673	34.2722	-5.1571	2.190	10.96	2.79	10.0	3.21 ± 0.58	U4-34817	10.7	0.00
U4-36568b ^e	34.2935	-5.1548	18.7	1.51 ± 0.21	U4-36568	1.5	...
U4-39404	34.5505	-5.1433	1.63	10.47	1.63	5.5	0.46 ± 0.22	U4-39126	4.6	0.40
GS4-10771	53.0785	-27.8599	3.6600	11.20	2.80	8.7	0.70 ± 0.25	GS4-11016	3.8	1.62
GS4-11466	53.0779	-27.8582	0.6465	10.62	1.37	6.4	0.72 ± 0.29	GS4-11016	5.4	1.39
GS4-14173	53.0702	-27.8455	3.70	10.34	1.98	18.7	2.12 ± 0.31	GS4-14747	8.3	1.74
GS4-23075	53.0923	-27.8032	2.72	11.02	2.47	25.9	2.87 ± 0.27	GS4-22825	6.6	0.35
GS4-23372	53.0928	-27.8012	2.93	10.65	2.14	18.6	3.86 ± 0.58	GS4-22825	11.2	0.56
GS4-41332	53.1100	-27.7168	3.10	10.20	2.27	10.8	1.66 ± 0.50	GS4-41181	10.8	0.80
GS4-44920	53.1388	-27.7005	2.4495	10.49	1.83	5.4	0.39 ± 0.18	GS4-45068	4.0	0.00
GS4-46181	53.1753	-27.6948	4.79	11.92	3.64	15.1	6.78 ± 0.92	GS4-45475	13.0	2.77

^a Redshifts with 5 digits are based on spectroscopic observations (Szokoly et al. 2004; Popesso et al. 2009; Kurk et al. 2013).

^b 3D-HST ID of the primary target in ALMA observations.

^c Projected separation between the serendipitously detected source and the primary target.

^d Redshift difference between the serendipitously detected source and the primary target.

^e U4-36568b is not detected in the HST image and is visible only in the ALMA 870 μm image.

Table 3
The 870 μm properties for 74 massive star-forming galaxies.

ID	$S_{\text{visibility}}$ (n=0.5) (mJy)	$R_{\text{e,FIR}}$ (n=0.5) (kpc)	q_{FIR} (n=0.5)	PA_{FIR} (n=0.5)	$S_{\text{visibility}}$ (n=1) (mJy)	$R_{\text{e,FIR}}$ (n=1) (kpc)
U4-190	5.05 \pm 0.09	0.9 \pm 0.1	0.71 \pm 0.07	79 \pm 7	5.18 \pm 0.10	0.8 \pm 0.0
U4-394	1.27 \pm 0.10	1.1 \pm 0.2	0.78 \pm 0.29	152 \pm 42	1.35 \pm 0.11	1.2 \pm 0.2
U4-1833	1.77 \pm 0.16	3.8 \pm 0.5	0.34 \pm 0.10	163 \pm 6	1.89 \pm 0.20	4.0 \pm 0.6
U4-2166	1.81 \pm 0.10	1.1 \pm 0.2	0.73 \pm 0.20	152 \pm 22	1.88 \pm 0.11	1.1 \pm 0.1
U4-2394	0.68 \pm 0.18	3.0 \pm 0.9	0.69 \pm 0.22	2.9 \pm 1.2
U4-4059	1.62 \pm 0.08	0.6 \pm 0.1	0.67 \pm 0.29	145 \pm 27	1.65 \pm 0.09	0.6 \pm 0.1
U4-4706	0.42 \pm 0.15	2.3 \pm 1.1	0.27 \pm 0.08	0.3 \pm 0.5
U4-4915	1.58 \pm 0.19	3.3 \pm 0.5	0.92 \pm 0.25	171 \pm 88	1.75 \pm 0.24	3.6 \pm 0.6
U4-7472	2.50 \pm 0.12	2.1 \pm 0.2	0.60 \pm 0.11	85 \pm 9	2.74 \pm 0.15	2.3 \pm 0.2
U4-7516	2.46 \pm 0.17	3.4 \pm 0.3	0.60 \pm 0.11	6 \pm 9	2.69 \pm 0.22	3.7 \pm 0.4
U4-9367	1.81 \pm 0.12	1.9 \pm 0.3	0.60 \pm 0.15	121 \pm 14	1.91 \pm 0.14	1.9 \pm 0.3
U4-12441	1.19 \pm 0.18	4.3 \pm 0.9	0.42 \pm 0.16	97 \pm 10	1.29 \pm 0.22	4.6 \pm 1.0
U4-13526	0.81 \pm 0.08	0.4 \pm 0.2	0.68 \pm 0.85	98 \pm 80	0.81 \pm 0.08	0.4 \pm 0.2
U4-13952	2.91 \pm 0.17	2.7 \pm 0.3	0.64 \pm 0.11	136 \pm 10	3.16 \pm 0.22	2.9 \pm 0.3
U4-14409	4.02 \pm 0.09	1.1 \pm 0.1	0.40 \pm 0.06	68 \pm 3	4.12 \pm 0.10	1.1 \pm 0.1
U4-14723	2.14 \pm 0.14	2.9 \pm 0.3	0.48 \pm 0.10	55 \pm 7	2.26 \pm 0.17	2.9 \pm 0.3
U4-14996	0.42 \pm 0.09	0.7 \pm 0.3	0.44 \pm 0.10	0.7 \pm 0.4
U4-16022	0.32 \pm 0.08	0.3 \pm 0.4	0.32 \pm 0.08	0.3 \pm 0.4
U4-16442	1.62 \pm 0.10	1.7 \pm 0.2	0.29 \pm 0.12	85 \pm 6	1.70 \pm 0.11	1.8 \pm 0.3
U4-16504	2.83 \pm 0.12	1.3 \pm 0.1	0.85 \pm 0.14	146 \pm 29	2.99 \pm 0.14	1.3 \pm 0.1
U4-16795	4.22 \pm 0.11	1.2 \pm 0.1	0.53 \pm 0.06	126 \pm 5	4.39 \pm 0.12	1.2 \pm 0.1
U4-17519	6.61 \pm 0.12	1.6 \pm 0.1	0.92 \pm 0.06	108 \pm 22	6.98 \pm 0.14	1.6 \pm 0.1
U4-19068	1.87 \pm 0.14	2.4 \pm 0.3	0.76 \pm 0.18	135 \pm 24	1.93 \pm 0.17	2.3 \pm 0.3
U4-19126	0.76 \pm 0.10	1.6 \pm 0.5	0.64 \pm 0.38	65 \pm 35	0.79 \pm 0.12	1.6 \pm 0.5
U4-20704	3.15 \pm 0.24	4.9 \pm 0.5	0.40 \pm 0.09	180 \pm 5	3.40 \pm 0.29	5.1 \pm 0.6
U4-21665	0.96 \pm 0.09	1.1 \pm 0.3	0.68 \pm 0.34	106 \pm 36	1.00 \pm 0.11	1.1 \pm 0.3
U4-21998	0.67 \pm 0.11	2.4 \pm 0.8	0.23 \pm 0.24	82 \pm 11	0.69 \pm 0.12	2.3 \pm 0.8
U4-22227	3.04 \pm 0.12	1.7 \pm 0.1	0.76 \pm 0.11	156 \pm 14	3.16 \pm 0.14	1.7 \pm 0.1
U4-22729	4.53 \pm 0.12	2.0 \pm 0.1	0.53 \pm 0.05	48 \pm 4	4.82 \pm 0.14	2.1 \pm 0.1
U4-23044	5.04 \pm 0.09	1.1 \pm 0.1	0.99 \pm 0.08	0 \pm 2	5.22 \pm 0.12	1.1 \pm 0.1
U4-23692	5.52 \pm 0.14	2.1 \pm 0.1	0.88 \pm 0.07	92 \pm 17	5.97 \pm 0.17	2.2 \pm 0.1
U4-26012	1.16 \pm 0.10	1.1 \pm 0.2	0.58 \pm 0.26	180 \pm 20	1.21 \pm 0.11	1.2 \pm 0.2
U4-26581	2.91 \pm 0.09	0.9 \pm 0.1	0.62 \pm 0.11	63 \pm 10	2.96 \pm 0.10	0.9 \pm 0.1
U4-28087	2.92 \pm 0.27	5.6 \pm 0.6	0.70 \pm 0.11	113 \pm 12	3.35 \pm 0.37	6.4 \pm 0.7
U4-28156	5.33 \pm 0.12	2.0 \pm 0.1	0.72 \pm 0.06	109 \pm 7	5.61 \pm 0.15	2.0 \pm 0.1
U4-28473	4.22 \pm 0.12	1.3 \pm 0.1	0.44 \pm 0.06	24 \pm 4	4.35 \pm 0.13	1.3 \pm 0.1
U4-28702	1.82 \pm 0.12	1.3 \pm 0.2	0.67 \pm 0.23	3 \pm 23	1.88 \pm 0.14	1.2 \pm 0.2
U4-29179	1.24 \pm 0.12	2.6 \pm 0.5	0.36 \pm 0.14	101 \pm 9	1.35 \pm 0.15	2.9 \pm 0.6
U4-31189	0.78 \pm 0.12	1.6 \pm 0.4	0.83 \pm 0.15	1.7 \pm 0.5
U4-32147	0.82 \pm 0.18	2.8 \pm 0.7	0.87 \pm 0.22	2.7 \pm 0.9
U4-32351	0.67 \pm 0.10	0.7 \pm 0.2	0.70 \pm 0.11	0.7 \pm 0.2
U4-32992	1.03 \pm 0.13	2.1 \pm 0.5	0.67 \pm 0.30	166 \pm 29	1.08 \pm 0.15	2.1 \pm 0.5
U4-34138	1.24 \pm 0.10	0.7 \pm 0.2	0.47 \pm 0.25	107 \pm 16	1.27 \pm 0.10	0.7 \pm 0.1
U4-34454	1.78 \pm 0.16	3.5 \pm 0.5	0.50 \pm 0.13	92 \pm 9	1.86 \pm 0.19	3.5 \pm 0.5
U4-34617	1.12 \pm 0.09	0.6 \pm 0.1	0.27 \pm 0.33	60 \pm 12	1.15 \pm 0.09	0.6 \pm 0.1
U4-34817	2.04 \pm 0.21	3.5 \pm 0.6	0.68 \pm 0.17	88 \pm 18	2.29 \pm 0.28	3.9 \pm 0.6
U4-36247	1.59 \pm 0.10	0.7 \pm 0.1	0.55 \pm 0.20	98 \pm 15	1.66 \pm 0.10	0.7 \pm 0.1
U4-36437	1.78 \pm 0.09	0.9 \pm 0.1	0.59 \pm 0.17	36 \pm 16	1.82 \pm 0.10	0.8 \pm 0.1
U4-36568	1.19 \pm 0.20	2.6 \pm 0.5	1.30 \pm 0.25	2.8 \pm 0.7
U4-36685	1.26 \pm 0.11	2.1 \pm 0.4	0.33 \pm 0.15	75 \pm 8	1.34 \pm 0.13	2.3 \pm 0.4
U4-37775	1.50 \pm 0.16	3.9 \pm 0.6	0.32 \pm 0.12	160 \pm 7	1.57 \pm 0.19	3.9 \pm 0.7
U4-38040	0.51 \pm 0.11	1.3 \pm 0.5	0.57 \pm 0.14	1.5 \pm 0.7
U4-38640	1.52 \pm 0.10	1.2 \pm 0.2	0.68 \pm 0.21	78 \pm 20	1.57 \pm 0.11	1.2 \pm 0.2
U4-39126	0.46 \pm 0.12	1.4 \pm 0.6	0.49 \pm 0.14	1.6 \pm 0.8
U4-39245	1.29 \pm 0.12	2.0 \pm 0.4	0.53 \pm 0.18	48 \pm 14	1.39 \pm 0.14	2.1 \pm 0.4
U4-40115	1.75 \pm 0.09	0.8 \pm 0.1	0.84 \pm 0.25	99 \pm 45	1.81 \pm 0.10	0.8 \pm 0.1
U4-42529	2.19 \pm 0.15	3.1 \pm 0.3	0.39 \pm 0.09	153 \pm 6	2.37 \pm 0.18	3.3 \pm 0.4
U4-42571	1.97 \pm 0.12	1.7 \pm 0.2	0.73 \pm 0.17	87 \pm 19	2.10 \pm 0.14	1.8 \pm 0.2
U4-42812	1.80 \pm 0.13	2.5 \pm 0.3	0.41 \pm 0.11	144 \pm 7	1.91 \pm 0.16	2.6 \pm 0.4
U4-43123	1.07 \pm 0.14	3.6 \pm 0.8	0.21 \pm 0.12	110 \pm 6	1.11 \pm 0.16	3.5 \pm 0.8
U4-43667	0.48 \pm 0.13	1.8 \pm 0.7	0.51 \pm 0.16	1.9 \pm 1.0
GS4-1725	1.00 \pm 0.19	1.7 \pm 0.4	1.04 \pm 0.23	1.7 \pm 0.5
GS4-4583	1.71 \pm 0.07	0.7 \pm 0.1	0.67 \pm 0.18	101 \pm 21	1.77 \pm 0.08	0.7 \pm 0.1
GS4-5217	1.50 \pm 0.15	2.8 \pm 0.5	0.58 \pm 0.19	48 \pm 17	1.69 \pm 0.19	3.2 \pm 0.5
GS4-11016	1.86 \pm 0.09	1.6 \pm 0.2	0.38 \pm 0.10	56 \pm 7	1.96 \pm 0.11	1.7 \pm 0.2
GS4-14747	2.24 \pm 0.08	0.6 \pm 0.1	0.85 \pm 0.17	152 \pm 32	2.31 \pm 0.08	0.6 \pm 0.1
GS4-19348	4.07 \pm 0.08	0.7 \pm 0.0	0.85 \pm 0.06	81 \pm 12	4.22 \pm 0.08	0.7 \pm 0.0
GS4-22825	1.34 \pm 0.09	1.1 \pm 0.2	0.65 \pm 0.16	129 \pm 16	1.43 \pm 0.10	1.2 \pm 0.2
GS4-30274	1.62 \pm 0.10	1.0 \pm 0.3	0.72 \pm 0.40	106 \pm 46	1.64 \pm 0.11	0.9 \pm 0.2
GS4-40185	0.36 \pm 0.06
GS4-41181	1.48 \pm 0.07	0.5 \pm 0.1	0.60 \pm 0.41	151 \pm 33	1.49 \pm 0.08	0.5 \pm 0.1
GS4-44065	0.82 \pm 0.11	2.2 \pm 0.7	0.39 \pm 0.23	103 \pm 15	0.86 \pm 0.13	2.3 \pm 0.7
GS4-45068	1.66 \pm 0.08	0.7 \pm 0.1	0.80 \pm 0.14	64 \pm 23	1.71 \pm 0.08	0.7 \pm 0.1
GS4-45475	1.06 \pm 0.24	5.0 \pm 1.0	1.13 \pm 0.31	5.1 \pm 1.4

Table 3 — *Continued*

ID	$S_{\text{visibility}} (n=0.5)$ (mJy)	$R_{\text{e,FIR}} (n=0.5)$ (kpc)	$q_{\text{FIR}} (n=0.5)$	$\text{PA}_{\text{FIR}} (n=0.5)$	$S_{\text{visibility}} (n=1)$ (mJy)	$R_{\text{e,FIR}} (n=1)$ (kpc)
----	--	-------------------------------------	--------------------------	----------------------------------	--	-----------------------------------